

New substellar candidates identified through deep learning in the F150 sample of the large-scale SHINE direct imaging survey

C. Cantero¹, M. Sabalbal², O. Absil^{2,*}, M. Van Droogenbroeck³, D. Ségransan¹, P. Delorme⁴

¹ Geneva Observatory, University of Geneva, Chemin Pegasi 51, 1290 Versoix, Switzerland

² STAR Institute, Université de Liège, Allée du Six Août 19C, 4000 Liège, Belgium

³ Montefiore Institute, Université de Liège, 4000 Liège, Belgium

⁴ IPAG, Univ. Grenoble Alpes, CNRS, Grenoble, France

Received September 15, 1996; accepted March 16, 1997

ABSTRACT

Context. The SPHERE High-contrast Imaging survey for Exoplanets (SHINE) represents one of the largest and most sensitive direct imaging campaigns conducted to date, targeting over 400 young, nearby stars with the goal of detecting and characterizing giant exoplanets and brown dwarfs. This extensive dataset offers a unique opportunity to revisit observations using modern, data-driven approaches, potentially uncovering new substellar candidates that may have been overlooked by classical analysis techniques.

Aims. In this context, our study focuses on reprocessing and reanalyzing the so-called F150 sample, a well-defined subset of 150 main-sequence stars within 100 pc observed in the H-band with VLT/SPHERE as part of the SHINE survey.

Methods. We apply NA-SODINN, a supervised deep learning model specifically tailored for detecting faint planetary signals in angular differential imaging (ADI) sequences. Designed to model local noise properties and capture spatial context, NA-SODINN is particularly effective at distinguishing real companions from residual speckle noise. To translate the model's pixel-wise confidence maps into actionable detections, we introduce a novel F1-score-based thresholding strategy. This principled approach balances sensitivity and specificity, addressing a key limitation in current deep learning-based methods.

Results. NA-SODINN recovers all known companions and some of the debris disks in the F150 sample, and identifies 13 new substellar candidates not reported in previous studies: ten detected in both the H2 and H3 bands, and three in only one band. For the ten sources detected in both bands, we use the H2–H3 color–magnitude diagram to perform a first assessment of their nature. Based on this analysis, we identify two ambiguous cases and three photometrically promising candidates. However, in light of the currently available multi-epoch SPHERE data, only the candidate around Smethells 20 remains a strong target for follow-up.

Key words. methods: data analysis – methods: statistical – techniques: image processing – techniques: high angular resolution – planets and satellites: detection

1. Introduction

Exoplanet direct imaging has become crucial for complementing indirect detection methods. Since the first direct detection of an exoplanet (Chauvin et al. 2004), the field of high contrast imaging (HCI) has become an essential tool not only for detecting young, self-luminous giant planets at wide separations (typically between 10 and 100 au) but also for enabling follow-up low-resolution spectroscopy of these objects, providing crucial insights into their chemical composition and atmospheric properties. Having access to this wide orbit space enables statistical analyzes that help constrain occurrence rates, shedding light on the initial conditions of protoplanetary disks (Janson et al. 2021), and serving as critical tracers of formation mechanisms and dynamical histories, ultimately refining current formation models (e.g., Bowler 2016).

To date, HCI has been able to detect around 60 substellar companions around young nearby stars, mostly thanks to the implementation of HCI surveys over the past two decades. Early surveys, with sample sizes of 50–100 stars, led to the discovery of some of the first planetary-mass companions at large separations (>100 au) or with low mass ratios relative to their host stars (i.e., Chauvin et al. 2004; Chauvin et al. 2005b; Neuhäuser

et al. 2005; Lafrenière et al. 2008). These discoveries paved the way for the detection of the most iconic directly imaged planetary systems, including HR 8799 bcde (Marois et al. 2008b) and β -Pictoris b (Lagrange et al. 2009). More recent large-scale surveys, such as the Gemini Planet Imager Exoplanet Survey (GPIES, Nielsen et al. 2019) and the SpHere INfrared survey for Exoplanets (SHINE, Chauvin et al. 2017), have expanded their sample sizes to 600 and 400 stars, respectively. So far, these new generation surveys have only led to the discovery of five giants, 51 Eri b (Macintosh et al. 2015), HIP 65426 b (Chauvin et al. 2017), PDS 70 b and c (Keppler et al. 2018), and HD143811 (AB)b (Squicciarini, V. et al. 2025), and some higher mass brown dwarfs (Konopacky et al. 2016; Cheetham et al. 2018). This relatively low number of HCI detections compared to expectations from radial velocity extrapolations (i.e., Cumming et al. 2008) is not solely indicative of a true absence of wide-orbit planets. Rather, it also highlights the substantial observational challenges, such as image contrast, that continue to limit the sensitivity of HCI surveys.

In HCI, contrast refers to the extreme flux ratio between a bright host star and its much fainter planetary companion. In the near-infrared, typical contrasts for young giant planets range from 10^{-4} to 10^{-6} . Achieving such contrasts using 8–10 meter ground-based telescopes requires a combination of precise

* F.R.S.-FNRS Research Director

instrumentation and advanced data processing. On the instrumental side, extreme adaptive optics (AO) systems and HCI instruments work in synergy during observations to correct for atmospheric turbulence and employ dedicated coronagraphs to suppress stellar light, respectively (Kenworthy & Haffert 2025). However, starlight is never perfectly removed in coronagraphic images. Residual wavefront errors and optical imperfections produce quasi-static speckles that can mimic planetary signals in both shape and brightness (Males et al. 2021). These limitations naturally lead to the algorithmic side, where observational strategies combined with image post-processing techniques are used to suppress these residual speckles, reach deeper contrasts, and recover companion signatures. The most widely used observing strategy on ground-based telescopes is angular differential imaging (ADI, Marois et al. 2006), in which coronagraphic images are acquired in pupil-tracking mode: the telescope pupil remains fixed while the image rotates over time due to the Earth’s rotation. As a result, speckles associated with the telescope and instrument optical train remain mostly fixed in the focal plane while the astrophysical signals rotate around the star as a function of the parallactic angle. This generates a sequence of coronagraphic images (ADI sequence, hereafter) that contains rich angular diversity and allows post-processing algorithms to effectively disentangle true planetary signals from residual image noise.

Over the past two decades, numerous image post-processing techniques have been developed to improve planet detection in ADI datasets (see Cantalloube et al. 2020, for a review). Among these, a major family relies on point spread function (PSF) subtraction. These methods aim to build a model of the stellar PSF from the ADI sequence and subtract it from each frame. The residuals are then derotated and combined based on their parallactic angles, producing a final image in which residual speckles are further attenuated and spatially decorrelated. This output is referred to as the processed frame. Among PSF subtraction techniques, principal component analysis (PCA, Soummer et al. 2012; Amara & Quanz 2012) and its extension, annular PCA (Absil et al. 2013; Gomez Gonzalez et al. 2016), have become standard approaches in major HCI surveys (e.g., Nielsen et al. 2019; Janson et al. 2021; Langlois et al. 2021). Their widespread use is largely due to several practical advantages: PCA is computationally efficient, has a solid mathematical foundation, requires minimal hyperparameter tuning (Bonse et al. 2024), and is currently integrated into major HCI pipelines such as VIP (Gomez Gonzalez et al. 2017; Christiaens et al. 2023), PynPoint (Stolker et al. 2019), and pyKLIP (Wang et al. 2015). Recently, machine learning, and in particular deep learning, has emerged as a powerful alternative that can be adapted to work in synergy with PSF subtraction techniques like PCA, delivering superior performance in tasks such as exoplanet signal detection (e.g., Gomez Gonzalez et al. 2018; Flasseur et al. 2024) and speckle noise modeling (Yip et al. 2020; Wolf et al. 2024). A notable example is NA-SODINN (Cantero et al. 2023), a recent supervised binary classifier based on convolutional neural networks (CNNs). It enhances detection sensitivity on ADI-PCA processed frames by learning deep spatio-temporal correlations of residual speckle noise across different noise regimes and incorporates signal-to-noise (S/N) curves as additional predictors, which provide complementary information about companion-like features. This multi-dimensional learning strategy has enabled NA-SODINN to outperform traditional techniques, securing top ranks in the first phase of the Exoplanet Imaging Data Challenge (EIDC, Cantalloube et al. 2020).

In this study, we aim to leverage the power of NA-SODINN to reprocess the F150 sample from the SHINE survey in search of new substellar candidates. To improve its applicability to large-scale survey analysis, we introduce two key modifications to the original pipeline: (1) an automated, F_1 -score-driven method for selecting optimal detection thresholds in each output map, enhancing interpretability and improving candidate selection; and (2) contrast curve generation to quantify detection sensitivity across the survey. Aside from these additions, the core algorithm remains unchanged. Thus, this work represents the first application of NA-SODINN to real data from a large-scale HCI survey, providing not only an opportunity to search for new companions but also to critically assess the algorithm’s performance, limitations, and future development paths.

This paper is structured as follows: Section 2 introduces the SHINE survey and its observing strategy, with a particular focus on the F150 sample used in this study. It also summarizes the current status of the full survey and the complementary snapSHINE program. Section 3 details the full data reduction process of the F150 sample, including image preprocessing, an overview of the NA-SODINN algorithm, the new thresholding strategy for candidate identification, the generation of final detection maps for each target, and the sensitivity analysis through contrast curves. Section 4 presents the detected candidate companions and their analysis. Finally, Section 5 discusses the implications of our results and summarizes the main conclusions.

2. SHINE survey

The SHINE survey (Chauvin et al. 2017) represents one of the most ambitious large-scale direct imaging campaigns. Conducted over 200 nights between February 2015 and September 2021, the survey was carried out in visitor mode at the Very Large Telescope (VLT) using the Spectro-Polarimeter High-contrast Exoplanet REsearch (SPHERE, Beuzit et al. 2019), combining its SAXO extreme adaptive optics system (Fusco et al. 2006) and its apodized pupil Lyot coronagraph (APLC, Soummer 2005). It targeted a statistically robust sample of over 400 young, nearby stars, with a comprehensive set of scientific objectives. These included the detection of new giant exoplanets and circumstellar disks, the characterization of the atmospheres of both newly discovered and previously known exoplanets, the investigation of giant planet formation mechanisms, and the study of the dynamical architecture of planetary systems.

Each observation spanned approximately one to two hours employing ADI. Observations were conducted in one of two SPHERE configurations: IRDIFS or IRDIFS-EXT. Both modes enable the simultaneous use of the InfraRed Dual-beam Imager and Spectrograph (IRDIS, Dohlen et al. 2008) and the Integral Field Spectrograph (IFS, Claudi et al. 2008; Mesa et al. 2015), offering complementary spectral coverage across near-infrared wavelengths. In IRDIFS mode, IFS captures data in the YJ spectral bands within a compact $1''.77 \times 1''.77$ field of view, while IRDIS operates in Dual-Band Imaging mode (DBI, Vigan et al. 2010) using the H2-H3 filter pair (DB-H23), providing a broader $11'' \times 11''$ field of view. In the extended IRDIFS-EXT mode, IFS expands its coverage to include the YJH bands, and IRDIS switches to the K1-K2 filter pair (DB-K12). This latter setup is particularly suited for detecting red, young L-type planets in nearby star-forming regions, such as HD 95086 b in Sco-Cen (Chauvin et al. 2018).

To date, SHINE has led to various discoveries: the giant exoplanet HIP 65426 b (Chauvin et al. 2017), the first unambiguous detection of the protoplanet PDS 70 b embedded in a protoplan-

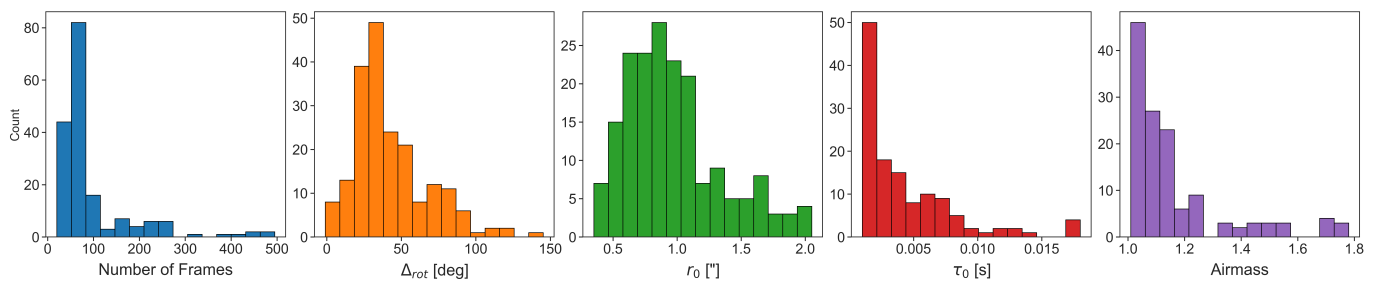


Fig. 1: Distributions of the main features extracted from the ADI sequences of the F150 sample. The number of frames in the sequence (blue) corresponds to the final value obtained after applying the Pearson correlation analysis described in Section 3.1. Δ_{rot} (orange) refers to the total field rotation during the sequence. The three rightmost panels correspond to atmospheric conditions: r_0 (green) indicates the mean seeing, τ_0 (red) the mean coherence time, and airmass (purple).

etary disk (Keppler et al. 2018), one brown dwarf (HIP 64892 B, Cheetham et al. 2018), four new disk detections (Lagrange et al. 2016; Feldt et al. 2017; Sissa et al. 2018; Perrot et al. 2019a), as well as 78 new stellar companions (Bonavita et al. 2022).

2.1. The F150 sample

An initial statistical analysis was performed on the first 150 targets observed between 2015 and 2017, referred to as the F150 sample¹. Fig. 1 shows the distribution of the main characteristics of the F150 sample. This subset was selected to be representative of the full survey and formed the basis of a trilogy of papers published in 2021.

In the first paper, Desidera et al. (2021) analyzed in detail the stellar properties of the F150 sample by combining indicators such as kinematics, moving group membership, lithium absorption, rotation periods, and chromospheric activity to estimate stellar ages and masses. The sample spans a broad range of spectral types, from B to M stars, with 53 BA stars, 77 FGK stars, and 20 M-type stars. The median age is 45 Myr, with 90% of the sample falling between 11 and 450 Myr. Stellar masses range from 0.57 to 2.37 M_{\odot} , with a median of 1.15 M_{\odot} , and the median distance is approximately 48 pc.

The observational setup and data processing for the F150 sample were presented in a second paper by Langlois et al. (2021). In total, 16 substellar companions were identified in the sample, eight brown dwarfs and eight planetary-mass companions, with most having been previously reported by earlier direct imaging campaigns. Additionally, 1483 candidate point sources were detected in the IRDIS field of view across all epochs using PCA through the SpeCal pipeline. Of these, 1176 were confirmed as background sources through follow-up observations or archival data, while 307 remained single-epoch detections and were considered as new candidates. Notably, more than 95% of these detections were obtained with the H2-H3 filter pair (DB-H23). Candidate prioritization was based on color-magnitude diagrams (CMDs), which led to the rejection of 44% of the H23 candidates as likely contaminants; ambiguous cases were scheduled for second-epoch follow-up.

Building upon these detection results, Vigan et al. (2021) carried out in a third paper a statistical analysis aimed at constraining the occurrence rates of wide-separation giant planets. By converting contrast curves to mass limits using evolutionary models and comparing the results with both parametric and pop-

ulation synthesis models, they derived occurrence rates across different spectral types.

2.2. Current status

With the completion of the initial F150 sample analysis, the SHINE survey advanced to its full statistical phase, expanding the sample to 400 stars and accumulating over 700 high-contrast datasets. This enlarged dataset significantly increased the number of detected point sources, mostly single-epoch detections with IRDIS in the H2-H3 filter pair. To discriminate between physical companions and background contaminants, the snapSHINE program was proposed. Unlike the deeper SHINE exposures designed for discovery and spectral characterization, snapSHINE was conceived as a rapid second-epoch astrometric follow-up survey. It used shorter exposure times and simplified observing sequences, enabling the confirmation or rejection of large numbers of candidates with minimal telescope time. While less sensitive than SHINE, snapSHINE was optimized to deliver reliable astrometric measurements at separations beyond $\sim 0.5''$, where most single-epoch sources are located.

As part of a new series of SHINE publications analyzing the full dataset, Chomez, A. et al. (2025) recently presented the observing strategy, data quality assessment, and point source analysis for the combined SHINE and snapSHINE samples. In a similar spirit to the earlier work of Langlois et al. (2021) on the F150 data, this new analysis applies the PACO-ASDI post-processing algorithm, which enhances contrast limits by up to two magnitudes. More than 3500 point sources were detected and classified in this (re)processing effort. Although no new confirmed exoplanets were identified, the improved sensitivity revealed 24 additional promising sources.

More recently, Sabalbal et al. (2026) reprocessed the F150 sample using RSM (Dahlqvist et al. 2020), a post-processing algorithm that achieved similarly top-ranked detection performance to NA-SODINN in the EIDC (Cantalloube et al. 2020). They reported a gain in median sensitivity of about a factor of two at $\sim 1''$ and of ~ 4 –5 at smaller angular separations relative to standard PCA, reaching performance comparable to PACO on the same datasets. Additionally, RSM yielded 87 detected signals, including 38 not recovered in the PACO-based analysis, and highlighted one particularly promising single-epoch candidate.

3. Methodology

This section describes the complete data reduction process applied to each ADI sequence of the F150 sample. It begins with

¹ The table with all the ADI sequences and their main characteristics, including atmospheric conditions, is available at the CDS via <https://cdsarc.cds.unistra.fr/viz-bin/cat/J/A+A/706/A275>

the initial SPHERE pre-processing steps, continues through the generation of final detection maps using the NA-SODINN algorithm, and concludes with the assessment of the survey’s sensitivity based on contrast curve analysis.

3.1. Raw data pre-processing

The SHINE F150 sample was pre-processed with the SPHERE data reduction and handling software (Pavlov et al. 2008), implemented at the High-Contrast Data Centre² (HC-DC, Maire et al. 2016; Delorme et al. 2017; Galicher et al. 2018; Beuzit et al. 2019). The initial reduction steps for the IRDIS data involved standard calibrations, including dark subtraction, flat-fielding, bad pixel correction, and background subtraction. Precise centering of the star was achieved using four satellite spots imprinted on the IRDIS images via a specific pattern applied to the deformable mirror. For each target in the sample, the output of this pre-processing is the ADI sequence with re-centered frames (individual detector integrations), along with the corresponding list of de-rotation angles required for ADI post-processing. For more details, including SPHERE calibration, we refer to Langelo et al. (2021).

3.2. Image processing

For this study, we considered two additional operations on each ADI sequence. First, each frame in the sequence is cropped to a 190×190 pixel region centered on the star, corresponding to a field of view radius of approximately $1''.2$. This inner region aligns with the area most effectively corrected by the SAXO extreme-AO system and where NA-SODINN has shown superior performance compared to standard PSF subtraction techniques (Cantero et al. 2023). Second, using the VIP Python package (Gomez Gonzalez et al. 2017; Christiaens et al. 2023), low-quality frames are identified and removed by computing the Pearson correlation between each frame and the median frame in the sequence. Frames with correlation values below 0.8 are discarded, as they potentially correspond to frames affected by poor AO correction or fast atmospheric variations. This threshold was chosen as a good trade-off between preserving data volume and filtering out frames that degrade post-processing performance. Both operations contribute to reducing the computational cost for the post-processing.

3.3. Advanced ADI post-processing

To search for companion candidates in each ADI sequence, we use the NA-SODINN (Cantero et al. 2023) post-processing algorithm, standing for Noise-Adaptive Supervised exOplanet detection via Direct Imaging with a deep Neural Network. It represents an upgraded version of SODINN (Gomez Gonzalez et al. 2018), its predecessor, and is a binary classifier model designed to distinguish between companion point-like signatures and residual noise in annular PCA residual frames (ADI-PCA processed frames, hereafter). In this section, we provide a brief overview of the NA-SODINN processing pipeline, which consists of four main steps. For a more detailed description, we refer to Cantero et al. (2023).

3.3.1. First step: Identification of noise regimes

Given an ADI sequence, the computation starts with a preliminary analysis of the residual noise distribution across the ADI-PCA processed frame. While this residual noise has often been (implicitly) assumed to be Gaussian—an assumption that produces high false positive detection rates (Marois et al. 2008a; Mawet et al. 2014) since it is not valid at small angular separations (Pairet et al. 2019; Dahlqvist et al. 2020; Daglayan et al. 2022, 2024)—NA-SODINN does not explicitly assume a specific probability distribution. Instead, it acknowledges that independent of the exact noise distribution, two non-overlapping noise regimes generally exist with different statistical properties: a non-Gaussian regime at small separations, dominated by residual speckle noise, and a Gaussian regime at larger separations, where speckle noise becomes smaller than background noise. NA-SODINN identifies and spatially delimits these noise regimes within the ADI-PCA processed frame. As detailed later in Section 3.3.2, this stratification strategy of the field of view enables the generation of independent training sets that accurately capture the statistical correlations of each noise distribution.

3.3.2. Second step: Generation of training sets

Once the noise regimes are identified, NA-SODINN proceeds with the generation of the training sets. For each regime, an independent dataset is created, consisting of two classes: the exoplanet class (c_+) and the noise class (c_-). Both classes are represented by hundreds of thousands of sequences of square image patches along with their corresponding signal-to-noise (S/N) curves (Fig. 2). These samples are generated annulus by annulus within each considered regime.

A c_+ patch sequence is generated through three consecutive actions. First, the instrumental PSF is injected³ at a random pixel within the considered noise regime. The flux of the injection is randomly selected such that the injection yields a S/N between 2 and 4 in the ADI-PCA processed frame produced with one single principal component. This modified ADI sequence is then processed using annular PCA with multiple k -subtraction levels (i.e., varying numbers of principal components). This results in k different ADI-PCA processed frames. Finally, from each of these, a square patch is cropped around the injection coordinates, forming a sequence of k patches that together constitute a single c_+ training sample (Fig. 2a). This sample contains local spatio-temporal pixel correlations of the synthetic injection that represent its evolution in PCA space (different k -subtraction levels). The associated S/N curve is computed following the definition from Mawet et al. (2014), measuring the S/N of the injection at each k -subtraction level. This curve encodes additional information about the interaction between the injected signal and the residual noise in the rest of the annulus (Cantero et al. 2023).

A c_- patch sequence and its S/N curve (Fig. 2b) are generated using the same procedure, except that no fake companion is injected. Since each ADI sequence yields only one realization of residual noise (per pixel), the number of c_- samples is limited to the total number of pixels in the annulus, which increases the risk of overfitting. To deal with this issue, NA-SODINN makes use of data augmentation techniques such as rotations, averages, and shifts to produce c_- training samples. As a result, these samples capture similar spatial and temporal correlations to the c_+

³ In HCI, a planetary injection is defined as the process of pasting the AO-corrected instrumental PSF (centered, cropped, and scaled to the desired contrast) to every frame in the ADI sequence at specific coordinates following field rotation.

² <https://hc-dc.cnrs.fr/?rubrique16&lang=en>

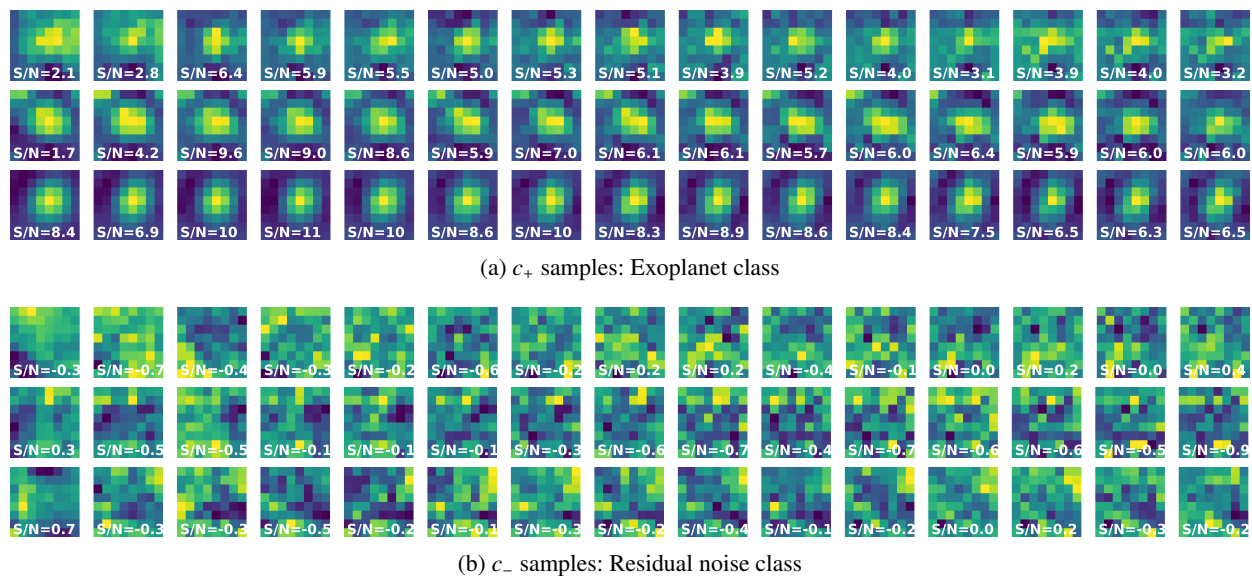


Fig. 2: Illustration of the training set used by NA-SODINN, showing three examples of patch sequences from the c_+ class (exoplanet, top) and three from the c_- class (residual noise, bottom). Each sample consists of a sequence of $N_k = 15$ image patches, each extracted from an ADI-PCA processed frame obtained with a different number of principal components, from $k = 2$ to $k = 30$ in steps of two. The S/N value displayed inside each patch is the S/N measured at the corresponding k , and the collection of these values across the sequence forms the associated S/N curve. For the c_+ class, the three samples are ordered by increasing injected flux, with injections selected such that the initial S/N at the first principal component $k = 1$ lies in the range 2–4. As k increases, the S/N typically rises at first as PCA better models and removes speckle noise, and then may decrease at higher k when the algorithm starts to subtract the planetary signal partially (self-subtraction). The patch size is set to twice the PSF FWHM (4 pixels in this case), resulting in 8×8 pixel patches.

class, but purely due to residual noise. The same number and order of k -subtraction levels are used as for the c_+ class to ensure the same noise subtraction in both classes.

3.3.3. Third step: Training

NA-SODINN continues by training a separate detection model for each noise regime using its corresponding training set. The network consists of two concatenated convolutional-LSTM blocks (Shi et al. 2015) with spatial 3D dropout (Srivastava et al. 2014) and MaxPooling-3D layers (Boureau et al. 2010), extracting spatio-temporal correlations from patch sequences. The resulting feature maps are flattened and concatenated with the corresponding S/N curves, forming a vector that also encodes S/N correlations. This vector is passed through a fully connected layer with 128 hidden units, a rectified linear unit (ReLU) activation function (Nair & Hinton 2010), and dropout regularization. The output layer consists of a sigmoid unit, providing a confidence score between 0 and 1. The network weights are initialized using a Xavier uniform initializer and optimized via backpropagation with a binary cross-entropy loss function. An Adam optimizer is employed with a learning rate of 0.003 and mini-batches of 64 training samples. Training is guided by an early stopping condition based on validation loss, with typically 7–10 epochs yielding ~ 99.9 validation accuracy.

3.3.4. Fourth step: Confidence map

The final stage of NA-SODINN involves applying the trained models to detect real companions in the same ADI sequence

used for training⁴. In the same fashion as the training set generation, inference is performed annulus by annulus within each corresponding noise regime. Given a pixel coordinate within a regime’s annulus, NA-SODINN first extracts the associated patch sequence and S/N curve. These inference samples are fed into the trained model corresponding to the pixel’s regime, which returns a confidence score between 0 and 1. This score reflects the model’s confidence that the pixel belongs to the c_+ class in such a way that higher scores (closer to 1) indicate likely companion detections, and lower scores point to regions dominated by residual noise. Repeating this process across the full field of view produces the confidence map: a pixel-level image aligned with the target’s field of view (i.e., Fig. 3-right), where companion detection can be performed by defining a confidence threshold.

3.4. Interpreting confidence maps

3.4.1. The confidence calibration problem

NA-SODINN is a data-driven framework designed to detect companion signatures in ADI sequences. This approach aims to offer two main advantages with respect to more standard post-processing techniques: (1) it achieves an improved balance between sensitivity and specificity across all angular separations and noise regimes (see Cantero et al. 2023), and (2) it aims to enhance interpretability through confidence maps that, unlike tradi-

⁴ In NA-SODINN, training and inference are performed on the same ADI sequence to ensure consistency of residual noise statistics. Since noise regimes are empirically defined and dataset-dependent, using external ADI sequences to build the c_- class and increase noise diversity could introduce domain mismatch effects. Noise diversity is instead achieved through data augmentation of the c_- class.

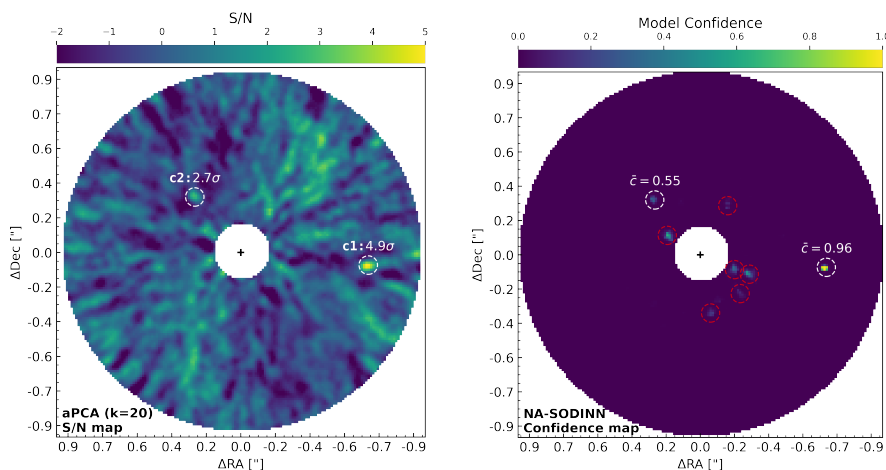


Fig. 3: Comparison between the S/N map (left), computed using annular PCA with $k = 20$ principal components, and the confidence map (right), computed using NA-SODINN trained with faint companion injections, for the *sph1* SPHERE ADI sequence from EIDC (Cantalloube et al. 2020). The small dashed circles in white indicate the true locations of the injected fake companions c1 and c2, while the red circles mark the positions of all NA-SODINN false positives if the detection threshold was set to a confidence score of 0.4 (see text). For both c1 and c2 injections, the S/N map highlights their sigma detection level while the confidence map shows the median confidence of all pixels located within a $1 - \lambda/D$ aperture. The circular concentric masked area with a radius of $\sim 3\lambda/D$ at the center of each image indicates the inner working angle.

tional processed frames or their S/N maps, provide a more homogeneous and reproducible basis for identifying candidate companions across different angular separations and noise regimes. Although both approaches ultimately rely on thresholding, confidence maps are based on patterns learned directly from the data rather than on residual intensities or S/N values alone.

However, confidence maps must be interpreted with caution. The confidence scores produced by binary classifiers, while bounded between 0 and 1 via a sigmoid activation (Section 3.3.3), do not represent calibrated probabilities (Tao et al. 2023) and therefore cannot be interpreted as such. Instead, they reflect the model’s internal certainty, which can be misleading. As a result, selecting an appropriate detection threshold cannot be based solely on intuition or on the assumption that a high score equates to a high probability of a true companion. This limitation becomes more pronounced when we aim to process large HCI surveys, such as the F150 sample, where NA-SODINN may flag numerous candidate companions with varying confidence levels.

Figure 3 illustrates this challenge, using the *sph1* SPHERE ADI sequence from the Exoplanet Imaging Data Challenge (Cantalloube et al. 2020). The left panel shows the S/N map obtained via annular PCA, where the two injected companions are highlighted with white circles: c1, located at a separation of ~ 650 mas with a significance of 4.9σ , and c2, at ~ 300 mas with a lower value of 2.7σ . In the corresponding NA-SODINN confidence map (right panel), c1 receives a high model confidence score $\bar{c} \sim 0.96$, while c2 is assigned a moderate score $\bar{c} \sim 0.55$. At first glance, this behavior might suggest a simple monotonic relation between apparent signal strength and model confidence: brighter companions receive higher scores, and fainter ones receive lower scores. However, the confidence map also contains several additional bright spots at similar separations (marked with red dashed circles) that are not associated with any injected companion. These false positives receive confidence scores in the same 0.4–0.6 range as c2, making them indistinguishable from a real detection based solely on raw confidence. This overlap illustrates a key issue: intermedi-

ate confidence values do not correspond to calibrated probabilities and cannot be directly interpreted as such. Without a principled thresholding mechanism, users are left to subjectively decide whether a pixel value like 0.55 represents a true companion or residual noise.

Several techniques have been proposed in the deep learning community to address this calibration problem. Overall, these can be categorized into three main groups. The first consists of post-hoc calibration methods, which aim to adjust model predictions after training by learning additional parameters on a held-out calibration dataset with the same properties as the training set. Examples include Platt scaling (Platt 1999), isotonic regression (Zadrozny & Elkan 2002), histogram binning (Zadrozny & Elkan 2001), Bayesian binning (Naeini et al. 2015), beta calibration (Kull et al. 2017), and temperature scaling (Guo et al. 2017). The second category involves regularization-based approaches that aim to improve calibration indirectly by enhancing model generalization. These include data augmentation techniques like Mixup (Thulasidasan et al. 2019) and AugMix (Hendrycks et al. 2020), ensemble methods (Lakshminarayanan et al. 2017), and explicit regularization strategies such as weight decay (Guo et al. 2017). Finally, the third category focuses on modifying the training loss function by introducing an auxiliary differentiable surrogate loss to approximate expected calibration error (Karandikar et al. 2021), or replacing the standard cross-entropy loss with alternatives such as mean squared error (Hui & Belkin 2021), inverse focal loss (Wang et al. 2021), or focal loss variants (Gupta et al. 2021).

While these approaches offer promising avenues for improving the interpretability of confidence maps, their adaptation to NA-SODINN is beyond the scope of this paper. Therefore, rather than interpreting confidence scores as probabilities, we adopt an alternative strategy tailored to the NA-SODINN architecture and for the analysis of the F150 sample: a threshold-optimization approach that seeks to identify, per annulus, the confidence value that maximizes detection performance. Specifically, this means selecting the confidence threshold that optimizes the trade-off

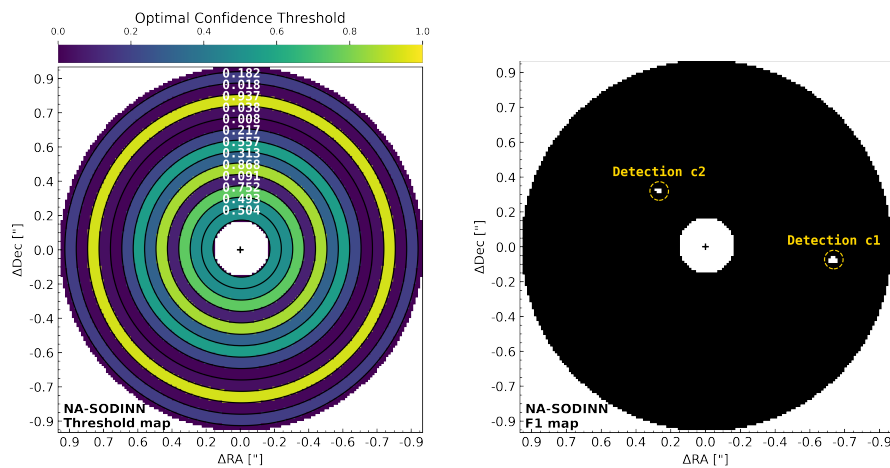


Fig. 4: Output of NA-SODINN’s proposed thresholding strategy for the *sph1* case shown in Fig. 3. *Left*: Threshold mask indicating the optimal confidence threshold per annulus, i.e., the value that maximizes the mean F_1 score across injection-recovery realizations. The overlaid white labels complement the colour map by showing the selected thresholds at each annulus. *Right*: Final binary detection map obtained by applying the threshold mask to the original confidence map of Fig. 3.

between false positives (FP) and false negatives (FN), on a per-dataset basis.

3.4.2. Defining robust confidence thresholds

In its original form, NA-SODINN performs inference annulus by annulus, scoring all pixels in the ADI sequence using the trained model corresponding to the local noise regime (Section 3.3.4). Once all pixels in an annulus are scored, NA-SODINN immediately proceeds to score all pixels in the next annulus without evaluating the reliability of the resulting confidence scores. In the proposed approach, this gap is addressed by introducing a dedicated injection-recovery step.

After scoring all pixels in a given annulus, NA-SODINN temporarily pauses inference and generates a set of $n = 50$ synthetic cubes, each created by duplicating the original ADI sequence and injecting two fake companions with random fluxes and positions restricted to the same annular region. Inference is then re-run on each of these n synthetic cubes, computing confidence scores only for the pixels within the target annulus. To assess detection performance, a dense grid of confidence thresholds between 0 and 1 is defined. For each threshold in the grid, the model’s outputs are compared with the known injection positions, allowing for the calculation of true positives (TPs), false positives (FPs), and false negatives (FNs). These basic indicators are then used to compute the F_1 -score (see Section A) at each threshold. This procedure yields an F_1 -score curve for every n realization, characterizing model performance as a function of the confidence threshold, as described in Sabalbal et al. (2026). Because the same number of fake companions is injected in each synthetic cube, the resulting individual F_1 scores are computed under the same number of positive priors, which allows their averaging to remain meaningful (Piérard & Van Droogenbroeck 2020). Averaging the n individual F_1 curves therefore provides a robust estimate of detection performance across thresholds, and the confidence value at which the mean curve reaches its maximum is selected as the optimal threshold for that annulus, as it offers the best trade-off between detection completeness and reliability.

This injection-recovery process is repeated independently for each annulus across the field of view. For each annulus, the confidence threshold corresponding to the maximum of the mean

F_1 curve is selected as the optimal value. These optimal thresholds are then used by NA-SODINN to construct a threshold map, an annulus-wise mask that assigns to each pixel the confidence threshold associated with its angular separation (Fig. 4, left). Applying this spatially varying threshold to the NA-SODINN confidence map yields what we refer to as the F_1 map: a binary detection map in which activated pixel blobs represent regions where the underlying signal meets the model’s strongest internal criteria for being distinguishable from noise, given the local noise regime and learned data characteristics. This approach resolves the ambiguity inherent in raw, uncalibrated confidence values by providing a clear and objective decision rule for detection. Figure 4-right shows the resulting F_1 map for the *sph1* dataset, which successfully recovers both injected companions (c1 and c2) without introducing any false positives.

3.5. Contrast curves

To assess the detection limits achieved by a post-processing algorithm in an HCI survey, contrast curves are typically computed from S/N maps using the standard 5σ criterion (e.g., Mawet et al. 2014; Langlois et al. 2021; Chomez, A. et al. 2025). In this approach, contrast is estimated at each angular separation from the computation of the noise standard deviation and the throughput.

NA-SODINN, however, produces confidence maps that assign a confidence score to each pixel rather than a flux-based S/N ratio. Since these confidence values do not follow the statistical assumptions underlying the classical 5σ framework, the standard definition of contrast cannot be applied consistently. Instead, we adopt an empirical completeness-based definition, following the injection-recovery philosophy of Dahlgvist et al. (2021). For each annulus, we first fix the detection threshold to the annulus-dependent confidence threshold derived in Section 3.4.2, which is the value that maximizes the F_1 -score. At each angular separation, 20 synthetic companions are then injected at different azimuths, and their fluxes are iteratively adjusted until NA-SODINN recovers 95% of them at this fixed threshold. A synthetic companion is considered recovered if it is detected at the expected location in the resulting binary detection map. The corresponding flux is taken as the contrast limit at that separation. This completeness-based contrast therefore provides an empirical estimate of the detection sensitivity of the

algorithm, without relying on assumptions about the underlying noise distribution.

4. Results

NA-SODINN was run separately on each preprocessed ADI sequence of the F150 sample. This involved, for every sequence, first identifying noise regimes (Section 3.3.1), and then, for each regime, generating training data (Section 3.3.2), training a ConvLSTM binary classifier (Section 3.3.3), and performing inference (Section 3.3.4), ultimately producing both confidence and F_1 maps (Section 3.4.2). Hereafter, we refer to both of them as detection maps. For targets with multiple observational epochs, each epoch was processed independently, meaning the full NA-SODINN pipeline was applied separately to each one. Similarly, H2 and H3 filter sequences for the same target were treated as distinct datasets.

A valid detection was defined as an ensemble of one or more connected pixels (Cantalloube et al. 2020) appearing in the confidence map, passing the threshold mask, and therefore also present in the F_1 binary map. Applying this criterion within our reduced field of view, NA-SODINN identified a total of 30 point-like candidate sources across 19 targets in the full survey, excluding confirmed gravitationally bound companions and disks. Some of these candidates had already been reported in previous studies, while others are newly identified here. To facilitate their analysis, this section is organized as follows. In Section 4.1, we review previously reported sources recovered by NA-SODINN, including confirmed substellar companions, detections previously classified as background contaminants or ambiguous cases in the literature, and known disks. In Section 4.2, we present the candidate sources not reported by earlier studies. Finally, Section 4.3 concludes with an evaluation of the sensitivity limits reached by NA-SODINN for the F150 sample.

Two appendices complement this section. A selection of NA-SODINN detection maps is provided in Section B, including some of the confirmed recovered planets and disks, as well as the candidate sources newly identified in this work. Section C summarizes the main properties of the target stars around which NA-SODINN identified new candidates (Table C.1), together with the characterization of the candidates themselves (Table C.2).

4.1. Previously reported discoveries

4.1.1. Known substellar companions

All confirmed companions present in the F150 sample were detected by NA-SODINN with high confidence scores. This includes the seven brown dwarfs PZ Tel B (Biller et al. 2010), HD 115470 B (Cheetham et al. 2018), η Tel B (Lowrance et al. 2000), CD-35 2722 B (Wahhaj et al. 2011), HD 143567 B (Lafrenière et al. 2011), HD 206893 B (Milli et al. 2017a), and CD-52 381 B (Chauvin et al. 2005a); as well as the nine planetary-mass companions 51 Eri b (Macintosh et al. 2015), β Pic b (Lagrange et al. 2009), HD 95086 b (Rameau et al. 2013), HR 8799 c, d, and e (Marois et al. 2008b, 2010), HD 116434 b (Chauvin et al. 2017), GJ 504 b (Kuzuhara et al. 2022), and AB Pic b (Chauvin et al. 2005b).

For illustrative purposes, Fig. B.1 presents four examples of these detections recovered in both the H2 and H3 filters. For instance, Fig. B.1a shows the case of HR 8799. We observe that the three giant planets HR 8799 c, d, and e are recovered by NA-SODINN, while planet b is not detected as it falls outside our reduced $1''/2$ field of view. The presence of low-mass inner

companion interior to HR 8799 e could help stabilize the system dynamically (Goździewski & Migaszewski 2014), although deep SPHERE observations have ruled out planets more massive than $\sim 3\text{--}4 M_{\text{Jup}}$ in the 7.5–10 au range (Wahhaj et al. 2021). In Fig. B.1a, aside from the detection of planets c, d, and e, the NA-SODINN confidence maps also reveal a few other blobs that did not pass the threshold mask. Notably, in the H3 filter, a cluster of pixels with ~ 0.8 confidence appears at a slightly smaller angular separation than planet e. Although this signal could be considered significant, we opted not to include it in our posterior analysis due to its non-detection in the H2 filter and the absence of a corresponding signal in other epochs. For the systems HIP 65426, PZ Tel, and β Pic, whose NA-SODINN detection maps are shown in Figs. B.1b to B.1d, the known substellar companions are robustly recovered within the considered field of view. No additional significant point-like sources are identified in the corresponding confidence or binary maps. The same result is obtained for the other analogous systems in the F150 sample, including the seven brown dwarf hosts and the three additional exoplanet host stars.

4.1.2. Background contaminants and ambiguous cases

Seventeen NA-SODINN detections correspond to candidate point sources previously reported by Langlois et al. (2021), Chomez, A. et al. (2025), and Sabalbal et al. (2026). In those studies, these sources were ultimately classified either as background contaminants or as ambiguous cases. Five of them were identified as background contaminants, around HD175726, HD151726, HD148055, and HD107821, based on their position in color-magnitude diagrams and/or rejection via the common proper-motion test. Six others were flagged as ambiguous, around HD113457, HD107301, OUPup, and HD326277, typically because the astrometric and/or photometric measurements were not sufficiently reliable for a robust assessment. The remaining six are found in systems with additional noteworthy structures: two lie beyond the debris disk of HD115600 (Fig. B.2b), and four are found in systems for which we also report new candidates (Section 4.2): three around HD168210 (Fig. B.3b) and one around HD 164249 (Fig. B.3f).

4.1.3. Known debris disks

The F150 sample includes twelve confirmed debris disks. Nine of these were previously known, corresponding to the targets: β Pic (Lagrange et al. 2019), NZ Lup (Boccaletti et al. 2019), HD 115600 (Gibbs et al. 2019), HD 197481 (Boccaletti, A. et al. 2018), HD 15115 (Engler et al. 2019), HD 61005 (Olofsson et al. 2016), HD 377 (Choquet et al. 2016), CE Ant (Olofsson et al. 2018), and HD 109573 (Milli et al. 2017b). The remaining three, HD 160305 (Perrot et al. 2019b), HD 106906 (Lagrange et al. 2016), and HD 131835 (Feldt et al. 2017), were discovered within the SHINE survey. These disks were typically found around young stars, with a median stellar age of 24 Myr, and are most often observed at high inclinations, with a median value of $i = 82^\circ$ (Langlois et al. 2021), except for the case of CE Ant, which was detected at low inclination through polarimetric differential imaging (Olofsson et al. 2018). This prevalence of high-inclination detections is likely due to a selection bias introduced by ADI, which favored the detection of edge-on, optically thin disks through enhanced forward scattering and improved contrast performance.

Given our smaller field of view and the fact that the NA-SODINN neural network is trained to identify point-like sources rather than extended sources, we recovered, as shown in Fig. B.2, partial disk morphologies in only three of these systems. For example, Fig. B.2a shows the case of HD 109573, an A0V star with an estimated age of 10 ± 3 Myr (Bell et al. 2015) and at a distance of 71.91 ± 0.70 pc (Gaia Collaboration et al. 2023), that harbors one of the disks with the highest fractional luminosity, shaped as a thin ring of semi-major axis ~ 77 au inclined by $\sim 76^\circ$. We can observe that the NA-SODINN recovery of the disk morphology in both filters is surprisingly good, with very high confidence scores and no additional spurious detections. We attribute this unexpected result to the interplay between the S/N curves included during training (see Section 3.3.2) and their correlation with the patch sequence. Although the c_+ patch sequences contained only centered point-like source injections of varying fluxes and different noise levels, and no extended structures, the exceptionally high flux of HD109573’s disk produced strong S/N values across the corresponding S/N curves. This allowed the network to almost recover the full disk despite its lack of explicit training on extended features.

Figure B.2b presents the case of HD 115600, an F2V/F3V star with an estimated age of ~ 15 Myr and located at 109.6 ± 0.5 pc (Gaia Collaboration et al. 2023). This system harbors a smaller debris disk with a semi-major axis of ~ 48 au and an inclination of $\sim 79^\circ$. In contrast to HD109573, we observe that NA-SODINN struggles to recover the complete morphology of this disk, leaving significant gaps along its structure. Here, part of the disk lies within the speckle-dominated regime. As a result, despite the disk being intrinsically bright, the lower and more irregular S/N response in this area prevents the network from confidently identifying the entire ring, limiting the recovery to fragmented portions of the disk.

Finally, Fig. B.2c shows HD 197481 (AU Mic), an M3IVe star at 9.725 ± 0.005 pc that hosts two confirmed hot Neptunes (Plavchan et al. 2020; Martioli, E. et al. 2020) and possibly a third planet (Wittrock et al. 2023). Its edge-on disk, one of the largest and brightest known, extends from 40 to 120 au. In this case, NA-SODINN detects only a minor portion of the disk and no substellar candidates.

4.2. New candidates

In addition to the known companions, our analysis revealed 13 new candidates around 11 stars not previously reported in the literature. Table C.1 provides the main properties of these stars. We group these detections into two categories: 10 candidates detected in both H2 and H3 bands, including Smethells 20 (three candidates), HD 168210, π Ara, CD-51 10924, β Leo, HD 164249, CD-57 1054, and CE Ant; and 3 candidates detected in only one of the two bands, namely CD-48, HD 55279, and HD 219482. Figures B.3 and B.4 show the NA-SODINN detection maps for both groups, respectively.

The relative astrometry and photometry of these new candidates were estimated using the negative fake companion method (NEGFC, Wertz et al. 2017), as implemented in the VIP package (Gomez Gonzalez et al. 2017; Christiaens et al. 2023). Importantly, this characterization step is independent of NA-SODINN: while NA-SODINN was used to identify the candidate locations, the estimation of their astrometry and photometry relies solely on the signal present in the final ADI-PCA post-processed frame. Therefore, this procedure is only applicable to candidates that remain sufficiently visible after ADI-PCA processing. In practice, the method consists of injecting a fake companion with nega-

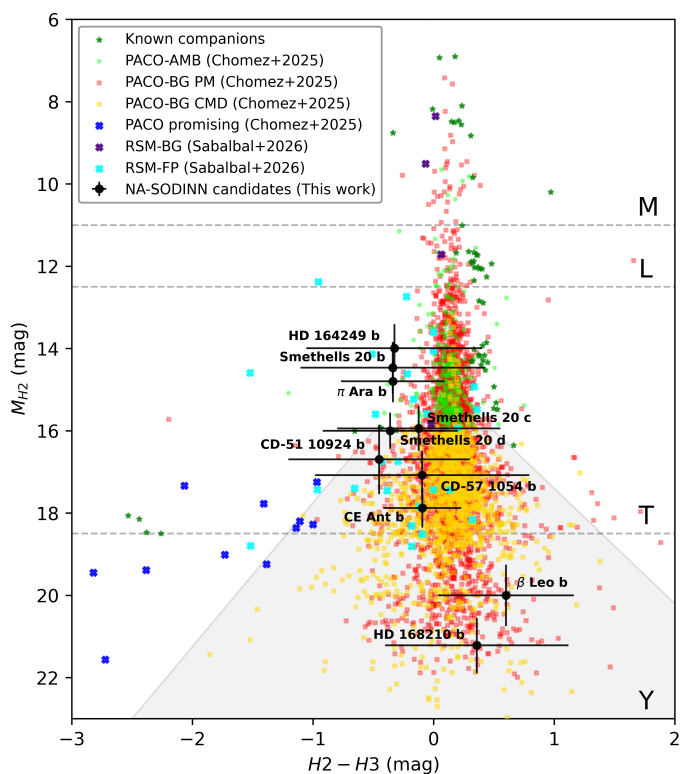


Fig. 5: H2–H3 color–magnitude diagram of the 10 NA-SODINN candidates detected in both bands (black circles with photometric uncertainties and labels). Previously known SHINE companions are shown as green stars. Candidate sources reported by Chomez, A. et al. (2025) and Sabalbal et al. (2026) are overplotted and colour-coded according to their final classification: ambiguous (PACO-AMB; light green), background contaminants rejected through proper-motion analysis (PACO-BG PM; red), background contaminants rejected through the CMD (PACO-BG CMD; yellow), promising candidates from PACO (PACO promising; blue), additional background sources identified by RSM (RSM-BG; purple), and RSM false positives (RSM-FP; aqua). The grey shaded region indicates the empirical background-exclusion zone defined by Chomez, A. et al. (2025), while horizontal dashed lines and labels mark approximate spectral-type transitions.

tive flux at the approximate location of the detected candidate in the ADI sequence. If the injected negative source has the correct position and flux, it will cancel the candidate signal in the ADI-PCA post-processed frame. To achieve this, the separation, position angle, and flux of the negative companion were adjusted through an iterative procedure that involved two steps. First, a Nelder-Mead simplex algorithm was used to obtain initial estimates. Second, these estimates were refined, and statistical uncertainties were obtained by sampling the posterior distributions with an MCMC sampler. Table C.2 presents this characterization for all the new candidates.

After deriving the astrometry and photometry, we placed the 10 candidates detected in both bands on a color–magnitude diagram (CMD; Fig. 5; see also Bonnefoy et al. 2018) to evaluate their nature. The CMD is a well-established diagnostic for distinguishing substellar companions from background contaminants, particularly beyond the L/T transition where silicate and iron clouds dissipate and methane absorption dominates, producing the characteristic blueward shift of T dwarfs. Following Chomez,

A. et al. (2025), we also show the empirically defined exclusion region that traces the locus of the dominant SHINE contaminants (field K- and M-type stars). For context, Fig. 5 additionally includes the population of previously confirmed SHINE companions, as well as the candidate detections reported by Chomez, A. et al. (2025) and Sabalbal et al. (2026), using PACO and RSM algorithms, respectively, color-coded by their final classifications. Note that the RSM signals presented in this diagram represent an updated version of the results published in Sabalbal et al. (2026), with signal characterization now performed using NEGFC.

Based on their photometric and astrometric properties, we preliminarily classify our candidates into three categories: (i) *background*, when the source is unlikely to be physically bound to the host star and is most probably a field star projected by chance within the field of view (see Section 4.2.1); (ii) *ambiguous*, when the available measurements do not allow a clear distinction between a background contaminant and a bound companion, often due to large uncertainties or conflicting indicators (see Section 4.2.2); and (iii) *promising*, when the source properties are consistent with expectations for substellar companions, making it a plausible bound object and, therefore, a good target for follow-up observations (see Section 4.2.3). The three candidates detected in only one band cannot be placed on the H2–H3 CMD and are therefore left *undefined* at this stage. This classification is also highlighted in Table C.2 and in NA-SODINN detection maps of Figs. B.3 and B.4.

4.2.1. Background

Substellar candidates labeled as background contaminants are those that fall within the exclusion region in the CMD of Fig. 5. We identify five clear cases: HD168210 b, β Leo b, CE Ant b, CD-57 1054 b, and CD-51 10924 b.

The HD 168210 system (Perugini et al. 2021) has been the subject of several HCI surveys, including the VLT/NaCo Large Program (Chauvin, G. et al. 2015) and the International Deep Planet Survey (Galicher, R. et al. 2016), which reported multiple candidate sources that were later confirmed as background stars. In our analysis, NA-SODINN recovers four sources (see Fig. B.3b): three of them match previously reported background contaminants, while an additional candidate, HD168210b, is detected with very high confidence (~ 0.98) at a projected separation of $\sim 569 \pm 20$ mas. In the CMD, this source falls well inside both empirical exclusion regions and overlaps the locus of background stars.

A similar situation is found in β Leo (HIP 57632), a bright A3V star with a prominent infrared excess from circumstellar dust (e.g., Cote 1987). NA-SODINN recovers a single candidate at $\sim 373 \pm 24$ mas (Fig. B.3e), detected with high confidence (~ 0.97). However, its photometry lies squarely within the exclusion region in the CMD, favoring a background interpretation. Moreover, β Leo has a very large proper motion (~ 500 mas/yr), so a stationary background source would be expected to show a substantial relative displacement with respect to the star between epochs and could therefore appear at noticeably different (and potentially larger) separations in earlier high-contrast imaging datasets. However, proper-motion vetting and dedicated follow-up observations are beyond the scope of this paper and are left for future work.

CE Ant (TWA 7) is an M2 star and a member of the TW Hydra young association (Webb et al. 1999). It hosts a nearly pole-on debris disk with multiple rings (Choquet et al. 2016; Ren et al. 2021), and recently Lagrange et al. (2025b) reported the direct imaging of a cold, sub-Jovian planet at $\sim 1''5$ with

JWST/MIRI—well outside our reduced field of view. Within our data, NA-SODINN recovers a point-like source at $\sim 328 \pm 28$ mas (Fig. B.3h), whose photometry lies securely within the exclusion regions of the CMD, again pointing to a background contaminant.

Among the young moving group members, CD-57 1054 (HIP 23309) stands out as a nearby M0 dwarf associated with the β Pic moving group (Lee & Song 2024). This star has been the focus of several exoplanet searches, including SHINE; however, no companions have yet been confirmed. Recently, Gollotti et al. (2024) identified two dips in TESS light curves that suggest a possible planet, but follow-up HARPS radial velocities remain inconclusive. In this context, the NA-SODINN detection maps (Fig. B.3g) reveal several faint features, of which only one meets the threshold mask criterion. The candidate, at $\sim 555 \pm 30$ mas, lies inside the inner exclusion region of the CMD, close to its boundary, with colors similar to CE Ant b. Its CMD placement favors a background interpretation.

The field M-dwarf CD-51 10924 (GJ 676 A) is part of a wide binary and hosts one of the most diverse planetary systems known around such stars. Forveille et al. (2011) first identified a massive companion (planet b) through radial-velocity monitoring and detected an additional long-term drift that could not be explained by the stellar companion GJ 676 B, suggesting the presence of a second giant planet c; this was later confirmed by Anglada-Escudé, G. & Tuomi, M. (2012), who also discovered two inner super-Earths (planets d and e) around GJ 676 A. In our NA-SODINN detection maps (Fig. B.3d), a point-like source is clearly recovered at a separation of $\sim 287 \pm 27$ mas in the single F150 epoch available for this target. In the CMD (Fig. 5), the source lies within the exclusion region. Astrometrically, the candidate would fall between planets b and c if bound, yet its brightness is inconsistent with such a scenario, favoring a background interpretation.

4.2.2. Ambiguous

Substellar candidates labeled as ambiguous are those that, within their photometric uncertainties, fall along the boundaries of the exclusion regions in Fig. 5. We identify two such cases: Smethells 20 c and d.

The young star Smethells 20 (or TYC 9073-762-1) is a member of the β Pictoris moving group (Binks & Jeffries 2017; Shan et al. 2017), and to date, no substellar companions have been confirmed in this system. Previous HCI surveys, including SHINE, as well as the MASSIVE program with VLT/NaCo (Lannier et al. 2016) and the Gemini/NICI Planet-Finding Campaign (Biller et al. 2013), reported additional candidate sources at wider separations, outside our reduced field of view, which were classified as background objects. However, as shown in Fig. B.3a, NA-SODINN identifies multiple candidate companions in the only epoch available in the F150 sample for this star. The two outer candidates, Smethells 20 c and d, at angular separations of $\sim 450 \pm 30$ mas and $\sim 680 \pm 28$ mas (see Table C.2), respectively, lie at the edge of the exclusion region in the CMD (Fig. 5). Their near-neutral colors are consistent with the L/T transition, with dust-free to moderately dusty atmospheres. If physically bound, their photometry is consistent with ~ 6 – $8 M_{\text{Jup}}$ companions according to the AMES-DUSTY evolutionary model, although their uncertainties also place them within the background locus, leaving their nature ambiguous.

4.2.3. Promising

Substellar candidates classified as promising are those that lie entirely outside the exclusion regions. We identify three such cases: Smethells 20 b, π Ara b, and HD 164249 b.

Unlike Smethells 20 c and d, the inner candidate (Fig. B.3a) detected at ~ 220 mas from the star (Table C.2), designated Smethells 20 b, lies outside the exclusion regions in Fig. 5. Within the photometric uncertainties, its position appears more consistent with ~ 9 – $11 M_{\text{Jup}}$ companions according to the AMES-DUSTY evolutionary model, while its relatively H2 - H3 color suggests the onset of CH_4 absorption in the near-IR, characteristic of young early-T substellar objects. No additional SPHERE epochs are currently available for an astrometric check of common proper motion. We also identified several archival NACO observations of this target, including a relatively deep L' pupil-tracking sequence, although the small angular separation of the candidate is likely to limit the constraining power of these data.

Figure B.3c presents the detection maps of the star π Ara (Zakhohay et al. 2022). In this case, NA-SODINN identifies a faint source at $\sim 900 \pm 25$ mas. To date, no bound companions have been confirmed around this system. Previous HCI, including HST/ACS coronagraphy (Doering et al. 2007), the SHINE survey, and the Gemini Planet-Finding Campaign (Wahhaj et al. 2013), likewise reported only background sources or non-detections. A second epoch, obtained on 2019-05-19 and available through the HC-DC, was also analyzed with NA-SODINN, but the candidate detected in the F150 epoch was not recovered.

The F6 star HD 164249 (HIP 88399) is a member of the β Pictoris moving group and hosts a known M2 stellar companion, HD 164249 B. An infrared excess, first detected with WISE (Wright et al. 2010), Spitzer (Chen et al. 2014), and Herschel (Eiroa et al. 2013), revealed the presence of a debris disk that was later spatially resolved with ALMA (Pawellek et al. 2021). Despite the absence of a direct detection in multiple SPHERE epochs (Mesa, D. et al. 2022), the star exhibits a significant proper motion anomaly indicative of an additional low-mass companion. Recent analyzes suggest the presence of a Jupiter-like planet with a mass of ~ 4 – $5 M_{\text{Jup}}$ at a semi-major axis of ~ 7 au (Gratton, R. et al. 2024; González-Payo, J. et al. 2024; Lagrange et al. 2025a), although this companion remains unconfirmed. The NA-SODINN detection maps reveal two point sources (Fig. B.3f): one located close to the outer edge of the field of view, which was also reported and classified as a background contaminant by Langlois et al. (2021), and another faint source at ~ 330 mas (~ 16 au). Although this latter detection does not coincide with the separation predicted for the putative low-mass companion inferred from astrometry, its position in the CMD (Fig. 5) overlaps with the locus of planetary-mass objects, making it an interesting candidate. However, five additional SPHERE epochs available through the HC-DC and obtained between 2015 and 2019 were also analyzed with NA-SODINN, and the same candidate was not recovered in any of them.

4.3. Sensitivity limits

As a final step in the reprocessing of the F150 sample with NA-SODINN, we computed 95% completeness contrast curves for each target following the procedure described in Section 3.5. The resulting curves in the IRDIS H2 and H3 filters are shown in Fig. 6. Beyond the inner working angle (~ 200 mas), the median

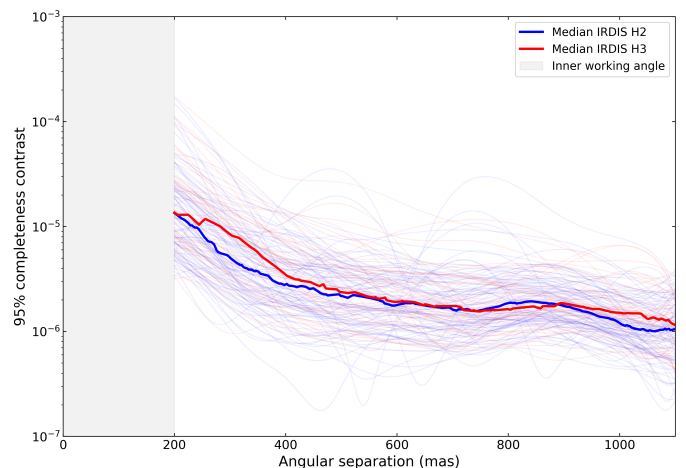


Fig. 6: NA-SODINN contrast curves, based on 95% completeness, computed for the set of ADI sequences in the F150 sample in both H2 (blue) and H3 (red) pass band filters. Thin curves represent individual sequences, while the thick curves correspond to the median contrast curve in each band. The gray shaded region marks the inner working angle.

95% completeness contrast improves rapidly, reaching $\sim 10^{-5}$ at ~ 250 mas in both filters, with slightly deeper limits in H2. At $\sim 1''$, the median contrast reaches values close to $\sim 10^{-6}$ in both H2 and H3.

As discussed in Section 3.5, these limits are not directly equivalent to standard 5σ contrast curves. Nevertheless, a comparison with previous IRDIS results obtained with PCA (Langlois et al. 2021), PACO (Chomez, A. et al. 2025), and RSM (Sababab et al. 2026) remains informative at the survey level. Relative to those methods, the NA-SODINN contrast curves exhibit a markedly reduced target-to-target dispersion over the full separation range. In terms of sensitivity gain, NA-SODINN appears broadly comparable to RSM within the reduced field of view explored here, and therefore also to PACO, given the similar performance reported for RSM and PACO in that separation regime.

5. Conclusions

In this work, we presented a reanalysis of the F150 sample (Desidera et al. 2021; Langlois et al. 2021; Vigan et al. 2021) from the SPHERE High-contrast Imaging survey for Exoplanets (SHINE, Chauvin et al. 2017) using the recently developed deep-learning detection algorithm NA-SODINN (Cantero et al. 2023). Given NA-SODINN's proven ability to discriminate faint substellar companions from residual speckle noise in ADI-PCA processed frames, our objective was to search for additional companion candidates in this first public SHINE release that may have been missed by previous analyzes.

To achieve this, we introduced two new modifications to the algorithm. First, since NA-SODINN produces confidence maps with uncalibrated probabilities rather than standard S/N maps, we implemented a principled detection criterion based on an F_1 -score-driven thresholding strategy. This procedure masks the confidence map annulus by annulus, providing an objective criterion for companion detection. Second, to compute detection limits, we adopted contrast curves based on 95% completeness instead of the classical 5σ criterion, and we optimized NA-

SODINN pipeline to calculate these curves for each target in the survey.

Based on these improvements and within the broader context of recent SHINE re-analyses, we reprocessed the full F150 sample on a sequence-by-sequence basis, establishing NA-SODINN as a competitive deep-learning alternative to existing approaches, such as the original PCA-based processing by [Langlois et al. \(2021\)](#), the PACO-based full-survey reprocessing by [Chomez, A. et al. \(2025\)](#), and the RSM-based reprocessing of the F150 sample by [Sabalbal et al. \(2026\)](#). NA-SODINN recovered all previously known companions in the survey, detected part of the circumstellar disks, and identified 30 additional substellar candidates. Of these, 17 had already been reported in the aforementioned studies and classified as either background contaminants or ambiguous cases. The remaining 13 sources, found around 11 stars, are reported here for the first time. Among them, three were detected in only one of the two IRDIS H23 spectral bands, while 10 were identified in both. For these 10 sources, we used the H2-H3 color-magnitude diagram to obtain a first-order assessment of their nature, classifying them into three groups: five background contaminants, two ambiguous cases, and three photometrically promising companion candidates around the stars Smethells, π Ara, and HD 164249. However, only the candidate Smethells 20 b remains as promising based on the currently available data, while the non-recovery of π Ara b and HD 164249 b in additional SPHERE epochs weakens their candidacy.

This study represents the first application of NA-SODINN to real data from a large high-contrast imaging survey. It therefore provides a benchmark for validating the method on survey observations and highlights clear directions for improvement. First, the per-sequence reduction strategy proved effective, but at the expense of substantial computational cost: processing a single ADI sequence in one band with NA-SODINN typically requires 10-30 hours in its current CPU multiprocessing implementation. This cost depends mainly on the number of frames in the sequence and, in particular, on the computation of the contrast curve, which is the dominant bottleneck. Reducing this cost will likely require the adaptation of alternative computational strategies. For example, clustering-based approaches (e.g., [Dahlqvist et al. 2022](#); [Sabalbal et al. 2026](#)) could be used to group ADI sequences with similar characteristics (e.g., atmospheric conditions) and enable the training of a single NA-SODINN model per cluster rather than training a separate model for each sequence. Second, the presented reprocessing approach can be extended beyond the F150 sample. A natural next step would be to reanalyze the full SHINE survey, enabling a more comprehensive statistical assessment of the companion population, and to adapt the pipeline to other ground-based HCI programs such as Gemini-GPIES ([Nielsen et al. 2019](#)), NACO-ISPY ([Launhardt et al. 2020](#)), and SPHERE-BEAST ([Janson et al. 2021](#)).

The field of HCI is rapidly evolving with the development of powerful post-processing techniques based on diverse principles for speckle modeling, speckle suppression, and point-like source detection. Applying such algorithms to archival surveys represents a cost-effective strategy to maximize their scientific return, as demonstrated in this work. Our results illustrate the potential of deep-learning approaches not only to recover known companions but also to reveal previously undetected candidates, underscoring the importance of re-examining existing datasets with modern tools while preparing for the next generation of HCI instruments such as SAXO+ ([Galland et al. 2024](#)) and GPI 2.0 ([Chilcote et al. 2024](#)).

Acknowledgements. This work has been carried out within the framework of the National Center of Competence in Research PlanetS supported by the Swiss National Science Foundation. The authors would like to thank the open-source Python scientific community, and in particular the developers of the Keras deep learning library ([Abadi et al. 2016](#)) and the VIP high-contrast imaging package ([Gomez Gonzalez et al. 2017](#); [Christiaens et al. 2023](#)), which were key to this work. We also extend our gratitude to the Exoplanet Imaging Data Challenge community ([Cantalloube et al. 2020](#)) for fostering a collaborative environment and contributing valuable tools and benchmarks to the field of HCI. We thank the entire SPHERE consortium for their long-standing efforts in the design, operation, and continued support of the SPHERE instrument, which made this survey possible. This work has made use of the High Contrast Data Centre, jointly operated by OSUG/IPAG (Grenoble), PYTHEAS/LAM/CeSAM (Marseille), OCA/Lagrange (Nice), Observatoire de Paris/LESIA (Paris), and Observatoire de Lyon/CRAL, and is supported by a grant from Labex OSUG@2020 (Investissements d’avenir – ANR10 LABX56). This project has received funding from the European Research Council (ERC) under the European Union’s Horizon 2020 research and innovation program (grant agreement No 819155), and from the Wallonia-Brussels Federation (grant for Concerted Research Actions).

References

- Abadi, M., Barham, P., Chen, J., et al. 2016, in *USENIX Conf. Oper. Syst. Des. Implement. (OSDI)*, 265–283
- Absil, O., Milli, J., Mawet, D., et al. 2013, *A&A*, 559, 1
- Amara, A. & Quanz, S. P. 2012, *MNRAS*, 427, 948
- Anglada-Escudé, G. & Tuomi, M. 2012, *A&A*, 548, A58
- Bell, C. P. M., Mamajek, E. E., & Naylor, T. 2015, *MNRAS*, 454, 593
- Beuzit, J.-L., Vigan, A., Mouillet, D., et al. 2019, *A&A*, 631, 1
- Biller, B. A., Liu, M. C., Wahhaj, Z., et al. 2010, *ApJL*, 720, L82
- Biller, B. A., Liu, M. C., Wahhaj, Z., et al. 2013, *ApJ*, 777, 160
- Binks, A. S. & Jeffries, R. D. 2017, *MNRAS*, 469, 579
- Boccaletti, A., Thébault, P., Pawellek, N., et al. 2019, *A&A*, 625, A21
- Boccaletti, A., Sezestre, E., Lagrange, A.-M., et al. 2018, *A&A*, 614, A52
- Bonavita, M., Gratton, R., Desidera, S., et al. 2022, *A&A*, 663, A144
- Bonnefoy, M., Perraut, K., Lagrange, A. M., et al. 2018, *A&A*, 618, A63
- Bonse, M. J., Gebhard, T. D., Dannert, F. A., et al. 2024, *arXiv preprint arXiv:2406.01809*
- Boureau, Y.-L., Ponce, J., & LeCun, Y. 2010, in *Int. Conf. Mach. Learn. (ICML)*, Haifa, Israel, 111–118
- Bowler, B. P. 2016, *Publications of the Astronomical Society of the Pacific*, 128, 102001
- Cantalloube, F., Gomez-Gonzalez, C., Absil, O., et al. 2020, in *Adaptive Optics Systems VII*, ed. D. Schmidt, L. Schreiber, & E. Vernet (SPIE), 321
- Cantero, C., Absil, O., Dahlqvist, C.-H., & Van Droogenbroeck, M. 2023, *A&A*, 680, A86
- Chauvin, G., Desidera, S., Lagrange, A. M., et al. 2017, in *SF2A-2017: Proceedings of the Annual meeting of the French Society of Astronomy and Astrophysics*, ed. C. Reylé, P. Di Matteo, F. Herpin, E. Lagadec, A. Lançon, Z. Meliani, & F. Royer, Di
- Chauvin, G., Desidera, S., Lagrange, A.-M., et al. 2017, *A&A*, 605, L1
- Chauvin, G., Gratton, R., Bonnefoy, M., et al. 2018, *A&A*, 617, A76
- Chauvin, G., Lagrange, A.-M., Dumas, C., et al. 2004, *A&A*, 425, L29–L32
- Chauvin, G., Lagrange, A. M., Lacombe, F., et al. 2005a, *A&A*, 430, 1027
- Chauvin, G., Lagrange, A. M., Zuckerman, B., et al. 2005b, *A&A*, 438, L29
- Chauvin, G., Vigan, A., Bonnefoy, M., et al. 2015, *A&A*, 573, A127
- Cheetham, A., Bonnefoy, M., Desidera, S., et al. 2018, *A&A*, 615, A160
- Chen, C. H., Mittal, T., Kuchner, M., et al. 2014, *ApJS*, 211, 25
- Chilcote, J., Konopacky, Q., Hamper, R., et al. 2024, in *Ground-based and Airborne Instrumentation for Astronomy X*, ed. J. J. Bryant, K. Motohara, & J. R. D. Vernet, Vol. 13096, International Society for Optics and Photonics (SPIE), 1309699
- Chomez, A., Delorme, P., Lagrange, A.-M., et al. 2025, *A&A*, 697, A99
- Choquet, É., Perrin, M. D., Chen, C. H., et al. 2016, *ApJL*, 817, L2
- Christiaens, V., Gonzalez, C. A. G., Farkas, R., et al. 2023, *Journal of Open Source Software*, 8, 4774
- Claudi, R. U., Turatto, M., Gratton, R. G., et al. 2008, in *Society of Photo-Optical Instrumentation Engineers (SPIE) Conference Series*, Vol. 7014, *Ground-based and Airborne Instrumentation for Astronomy II*, ed. I. S. McLean & M. M. Casali, 70143E
- Cote, J. 1987, *A&A*, 181, 77
- Cumming, A., Butler, R. P., Marcy, G. W., et al. 2008, *Publications of the Astronomical Society of the Pacific*, 120, 531–554
- Daglayan, H., Vary, S., Absil, O., et al. 2024, *A&A*, 692, A126
- Daglayan, H., Vary, S., Cantalloube, F., Absil, P.-A., & Absil, O. 2022, in *Int. Conf. Image Process. Appl. Syst. (IPAS)*, 1–5

- Dahlqvist, C.-H., Cantalloube, F., & Absil, O. 2020, *A&A*, 627, 1
- Dahlqvist, C.-H., Louppe, G., & Absil, O. 2021, *A&A*, 646, 1
- Dahlqvist, C. H., Milli, J., Absil, O., et al. 2022, *A&A*, 666, A33
- Delorme, P., Meunier, N., Albert, D., et al. 2017, in *Annual meeting of the French Society of Astronomy and Astrophysics (SF2A)*
- Desidera, S., Chauvin, G., Bonavita, M., et al. 2021, *A&A*, 651, A70
- Doering, R. L., Meixner, M., Holfeltz, S. T., et al. 2007, *AJ*, 133, 2122
- Dohlen, K., Langlois, M., Saisse, M., et al. 2008, in *Ground-based and Airborne Instrumentation for Astronomy II*, Vol. 7014, 70143L
- Eiroa, C., Marshall, J. P., Mora, A., et al. 2013, *A&A*, 555, A11
- Engler, N., Boccaletti, A., Schmid, H. M., et al. 2019, *A&A*, 622, A192
- Feldt, M., Olofsson, J., Boccaletti, A., et al. 2017, *A&A*, 601, A7
- Flasseur, O., Bodrito, T., Mairal, J., et al. 2024, *MNRAS*, 527, 1534
- Forveille, T., Bonfils, X., Lo Curto, G., et al. 2011, *A&A*, 526, A141
- Fusco, T., Rousset, G., Sauvage, J.-F., & Petit, C., et al. 2006, *Optics Express*, 14, 7515
- Gaia Collaboration, Vallenari, A., Brown, A. G. A., et al. 2023, *A&A*, 674, A1
- Galicher, R., Boccaletti, A., Mesa, D., et al. 2018, *A&A*, 615, A92
- Galicher, R., Marois, C., Macintosh, B., et al. 2016, *A&A*, 594, A63
- Galland, N., Raynaud, H.-F., Kasper, M., et al. 2024, in *Adaptive Optics Systems IX*, ed. K. J. Jackson, D. Schmidt, & E. Vernet, Vol. 13097, International Society for Optics and Photonics (SPIE), 1309711
- Gibbs, A., Wagner, K., Apai, D., et al. 2019, *AJ*, 157, 39
- Gollotti, G. A., Tzanidakis, A., Wainer, T. M., & Davenport, J. R. A. 2024, *Research Notes of the AAS*, 8, 293
- Gomez Gonzalez, C., Absil, O., Absil, P.-A., et al. 2016, *A&A*, 589, 1
- Gomez Gonzalez, C., Absil, O., & Van Droogenbroeck, M. 2018, *A&A*, 613, 1
- Gomez Gonzalez, C., Wertz, O., Absil, O., et al. 2017, *AJ*, 154, 7:1
- González-Payo, J., Caballero, J. A., Gorgas, J., et al. 2024, *A&A*, 689, A302
- Goździewski, K., & Migaszewski, C. 2014, *MNRAS*, 440, 3140
- Gratton, R., Bonavita, M., Mesa, D., et al. 2024, *A&A*, 685, A119
- Guo, C., Pleiss, G., Sun, Y., & Weinberger, K. Q. 2017, in *Int. Conf. Mach. Learn. (ICML)*, Vol. 70, 1321–1330
- Gupta, K., Rahimi, A., Ajanthan, T., et al. 2021, in *Int. Conf. Learn. Represent. (ICLR)*
- Hendrycks, D., Mu, N., Cubuk, E. D., et al. 2020, in *International Conference on Learning Representations*
- Hui, L., & Belkin, M. 2021, in *Int. Conf. Learn. Represent. (ICLR)*
- Janson, M., Siquicciarini, V., Delorme, P., et al. 2021, *A&A*, 646, A164
- Janson, M., Siquicciarini, V., Delorme, P., et al. 2021, *A&A*, 646, A164
- Karandikar, A., Cain, N., Tran, D., et al. 2021, in *Adv. Neural Inf. Process. Syst. (NeurIPS)*, ed. A. Beygelzimer, Y. Dauphin, P. Liang, & J. W. Vaughan
- Kenworthy, M. A., & Haffert, S. Y. 2025, *Annual Review of Astronomy and Astrophysics*, 63, 179
- Keppler, M., Benisty, M., Müller, A., et al. 2018, *A&A*, 617, 1
- Konopacky, Q. M., Rameau, J., Duchêne, G., et al. 2016, *ApJ*, 829, L4
- Kull, M., Silva Filho, T., & Flach, P. 2017, in *Int. Conf. Artif. Intell. Stat.*, 623–631
- Kuzuhara, M., Currie, T., Takarada, T., et al. 2022, *ApJL*, 934, 1
- Lafrenière, D., Jayawardhana, R., Janson, M., et al. 2011, *ApJ*, 730, 42
- Lafrenière, D., Jayawardhana, R., & van Kerkwijk, M. H. 2008, *AJ*, 689, L153
- Lagrange, A. M., Gratadour, D., Chauvin, G., et al. 2009, *A&A*, 493, L21
- Lagrange, A. M., Kiefer, F., Rubini, P., et al. 2025a, *arXiv e-prints*, arXiv:2501.10488
- Lagrange, A. M., Langlois, M., Gratton, R., et al. 2016, *A&A*, 586, L8
- Lagrange, A. M., Meunier, N., Rubini, P., et al. 2019, *Nature Astronomy*, 3, 1135
- Lagrange, A. M., Wilkinson, C., Mâlin, M., et al. 2025b, *Nature*, 642, 905
- Lakshminarayanan, B., Pritzel, A., & Blundell, C. 2017, in *Adv. Neural Inf. Process. Syst. (NeurIPS)* (Curran Associates Inc.), 6405–6416
- Langlois, M., Gratton, R., Lagrange, A.-M., et al. 2021, *A&A*, 651, A71
- Lannier, J., Delorme, P., Lagrange, A. M., et al. 2016, *A&A*, 596, A83
- Launhardt, Henning, Th., Quirrenbach, A., et al. 2020, *A&A*, 635, A162
- Lee, J. & Song, I. 2024, *AJ*, 967, 113
- Lowrance, P. J., Schneider, G., Kirkpatrick, J. D., et al. 2000, *ApJ*, 541, 390
- Macintosh, B., Graham, J. R., Barman, T., et al. 2015, *Science*, 350, 64
- Maire, A.-L., Langlois, M., Dohlen, K., et al. 2016, in *Ground-based and Airborne Instrumentation for Astronomy VI*, Vol. 9908, 990834
- Males, J. R., Fitzgerald, M. P., Belikov, R., & Guyon, O. 2021, *Publications of the Astronomical Society of the Pacific*, 133, 1
- Marois, C., Lafreniere, D., Doyon, R., Macintosh, B., & Nadeau, D. 2006, *ApJ*, 641, 556
- Marois, C., Lafreniere, D., Macintosh, B., & Doyon, R. 2008a, *ApJ*, 673, 647
- Marois, C., Macintosh, B., Barman, T., et al. 2008b, *Science*, 322, 1348
- Marois, C., Zuckerman, B., Konopacky, Q. M., Macintosh, B., & Barman, T. 2010, *Nature*, 468, 1080
- Martioli, E., Hébrard, G., Correia, A. C. M., Laskar, J., & Lecavelier des Etangs, A. 2020, *A&A*, 649, A177
- Mawet, D., Milli, J., Wahhaj, Z., et al. 2014, *ApJ*, 792, 1
- Mesa, D., Gratton, R., Zurlo, A., et al. 2015, *A&A*, 576, A121
- Mesa, D., Bonavita, M., Benatti, S., et al. 2022, *A&A*, 665, A73
- Milli, J., Hibon, P., Christiaens, V., et al. 2017a, *A&A*, 597, L2
- Milli, J., Vigan, A., Mouillet, D., et al. 2017b, *A&A*, 599, A108
- Naeni, M., Cooper, G., & Hauskrecht, M. 2015, *AAAI Conf. Artif. Intell.*, 2015, 2901
- Nair, V. & Hinton, G. 2010, in *Int. Conf. Mach. Learn. (ICML)*, Haifa, Israël, 807–814
- Neuhäuser, R., Guenther, E. W., Wuchterl, G., et al. 2005, *A&A*, 435, L13
- Nielsen, E. L., De Rosa, R. J., Macintosh, B., et al. 2019, *AJ*, 158, 1
- Olofsson, J., Samland, M., Avenhaus, H., et al. 2016, *A&A*, 591, A108
- Olofsson, J., van Holstein, R. G., Boccaletti, A., et al. 2018, *A&A*, 617, A109
- Pairet, B., Cantalloube, F., Gomez Gonzalez, C. A., Absil, O., & Jacques, L. 2019, *MNRAS*, 487, 2262
- Pavlov, A., Möller-Nilsson, O., Feldt, M., et al. 2008, in *Advanced Software and Control for Astronomy II*, Vol. 7019, 701939
- Pawellek, N., Wyatt, M., Matrà, L., Kennedy, G., & Yelverton, B. 2021, *MNRAS*, 502, 5390
- Perrot, C., Thebault, P., Lagrange, A.-M., et al. 2019a, *A&A*, 626, A95
- Perrot, C., Thebault, P., Lagrange, A.-M., et al. 2019b, *A&A*, 626, A95
- Perugini, G. M., Marsden, S. C., Waite, I. A., et al. 2021, *MNRAS*, 508, 3304
- Piérard, S., Deléglise, A., & Van Droogenbroeck, M. 2026, in *IEEE/CVF Conf. Comput. Vis. Pattern Recognit. (CVPR)* (IEEE)
- Piérard, S. & Van Droogenbroeck, M. 2020, in *IEEE Int. Conf. Image Process. (ICIP)* (IEEE), 3234–3238
- Platt, J. 1999, *Advances in large margin classifiers*, 10, 61
- Plavchan, P., Barclay, T., Gagné, J., et al. 2020, *Nature*, 582, 497
- Rameau, J., Chauvin, G., Lagrange, A.-M., et al. 2013, *ApJ*, 772, 2
- Ren, B., Choquet, É., Perrin, M. D., et al. 2021, *AJ*, 914, 95
- Sabalbal, M., Absil, O., Dahlqvist, C.-H., & Delorme, P. 2026, *A&A*, 706, A275
- Shan, Y., Yee, J. C., Bowler, B. P., et al. 2017, *ApJ*, 846, 93
- Shi, X., Chen, Z., Wang, H., et al. 2015, in *Adv. Neural Inf. Process. Syst. (NeurIPS)*, Vol. 1, 802–810
- Sissa, E., Olofsson, J., Vigan, A., et al. 2018, *A&A*, 613, L6
- Soummer, R. 2005, *ApJL*, 618, 161
- Soummer, R., Pueyo, L., & Larkin, J. 2012, *ApJL*, 755, 1
- Squicciarini, V., Mazoyer, J., Wilkinson, C., et al. 2025, *A&A*, 702, L10
- Srivastava, N., Hinton, G., Krizhevsky, A., Sutskever, I., & Salakhutdinov, R. 2014, *J. Mach. Learn. Res.*, 15, 1929
- Stolker, T., Bonse, M. J., Quanz, S. P., et al. 2019, *A&A*, 621, A59
- Tao, L., Dong, M., & Xu, C. 2023, in *Int. Conf. Mach. Learn. (ICML)*, PMLR, 33833–33849
- Thulasidasan, S., Chennupati, G., Bilmes, J., Bhattacharya, T., & Michalak, S. 2019, *On mixup training: improved calibration and predictive uncertainty for deep neural networks* (Curran Associates Inc.), 1–12
- Vigan, A., Fontanive, C., Meyer, M., et al. 2021, *A&A*, 651, A72
- Vigan, A., Moutou, C., Langlois, M., et al. 2010, *MNRAS*, 407, 71
- Wahhaj, Z., Liu, M. C., Biller, B. A., et al. 2011, *ApJ*, 729, 139
- Wahhaj, Z., Liu, M. C., Nielsen, E. L., et al. 2013, *AJ*, 773, 179
- Wahhaj, Z., Milli, J., Romero, C., et al. 2021, *A&A*, 648, A26
- Wang, D.-B., Feng, L., & Zhang, M.-L. 2021, in *Advances in Neural Information Processing Systems*, ed. A. Beygelzimer, Y. Dauphin, P. Liang, & J. W. Vaughan
- Wang, J. J., Ruffio, J.-B., De Rosa, R. J., et al. 2015, *pyKLIP: PSF Subtraction for Exoplanets and Disks*, *Astrophysics Source Code Library*, record ascl:1506.001
- Webb, R. A., Zuckerman, B., Platais, I., et al. 1999, *ApJ*, 512, L63
- Wertz, O., Absil, O., Gómez González, C. A., et al. 2017, *A&A*, 598, A83
- Wittrock, J. M., Plavchan, P. P., Cale, B. L., et al. 2023, *AJ*, 166, 232
- Wolf, T., Jones, B., & Bowler, B. 2024, *AJ*, 167, 92
- Wright, E. L., Eisenhardt, P. R. M., Mainzer, A. K., et al. 2010, *AJ*, 140, 1868
- Yip, K. H., Nikolaou, N., Coronica, P., et al. 2020, in *Lect. Notes Comput. Sci.*, Vol. 11908, *Joint European Conference on Machine Learning and Knowledge Discovery in Databases* (Springer Int. Publ.), 322–338
- Zadrozny, B. & Elkan, C. 2001, in *Int. Conf. Mach. Learn. (ICML)*, Vol. 1
- Zadrozny, B. & Elkan, C. 2002, in *ACM SIGKDD Int. Conf. Knowl. Discov. Data Min. (KDD)*, 694–699
- Zakhochay, O. V., Launhardt, R., Trifonov, T., et al. 2022, *A&A*, 667, L14

Appendix A: The F_1 -score

In a detection problem, such as exoplanet detection with NA-SODINN, each candidate can be assigned to one of four categories: true positive (TP), false positive (FP), or false negative (FN). These quantities form the basis for standard performance metrics such as *precision*, *recall* (also named *true positive rate*, TPR), and the F_1 -score.

In this work, a true positive corresponds to a detected injected planetary signal, while a false positive corresponds to a spurious detection caused by residual speckle noise or image artifacts. We assume that the analyzed data sets do not contain real astrophysical companions, such as genuine exoplanets or background stars, so that all positive detections can be unambiguously classified as either true or false.

Precision measures the fraction of positive detections that are correct, and is defined as

$$\text{Precision} = \frac{\text{TP}}{\text{TP} + \text{FP}}. \quad (\text{A.1})$$

It ranges from 0 to 1. A value close to 1 indicates that most detections correspond to injected planetary signals, with only a small number of false positives. However, optimizing only for high precision may lead to an overly conservative strategy in which faint or marginal signals are missed.

Recall, on the other hand, measures the fraction of injected signals that are successfully recovered:

$$\text{Recall} = \frac{\text{TP}}{\text{TP} + \text{FN}}. \quad (\text{A.2})$$

A high recall indicates that most injected companions present in the data are detected. In practice, however, increasing recall often comes at the expense of lower precision, since a more permissive detection criterion generally yields more false positives.

Because precision and recall are intrinsically coupled, the F_1 -score, defined as their harmonic mean, provides a convenient summary of the trade-off between the values of both quantities⁵:

$$F_1 = \frac{2 \cdot \text{Precision} \cdot \text{Recall}}{\text{Precision} + \text{Recall}} = \frac{2 \cdot \text{TP}}{2 \cdot \text{TP} + \text{FP} + \text{FN}}. \quad (\text{A.3})$$

A high F_1 -score indicates that the method achieves both high completeness and high reliability, that is, it recovers a large fraction of injected signals while keeping the number of false detections low. In the context of NA-SODINN, optimizing the detection threshold using the F_1 -score provides a practical compromise between precision and recall. This is particularly relevant in HCI, where the noise properties vary with angular separation and a single global threshold may not be optimal. By adapting the threshold on an annulus-by-annulus basis, the method yields a more robust and interpretable detection strategy.

Appendix B: NA-SODINN detection maps

In this appendix, we present all NA-SODINN detection maps for relevant targets in the F150 sample. The section is organized into figures, each grouping detection maps based on common

⁵ Note that, while F_1 is a good trade-off between the values of the precision and the recall, Piérard et al. (2026) have shown that F_1 is not necessarily a good trade-off between the ranks obtained for the precision and the recall. In other words, F_1 is adequate for optimizing a method, as we do, but not necessarily for comparing algorithms.

features among the targets. Figures B.1 and B.2 present detection maps for targets with confirmed substellar companions and known protoplanetary disks, respectively. Figures B.3 and B.4 display the maps for targets where new companion candidates were identified based on the detection criteria defined in Section 3.4.2. Detection maps for the remaining targets are omitted, as they are largely empty and contain no detections.

Appendix C: Characterization of substellar candidates

In this appendix, we summarize the main properties of the target stars around which NA-SODINN identified new candidates (Table C.1), together with the characterization of the candidates themselves (Table C.2).

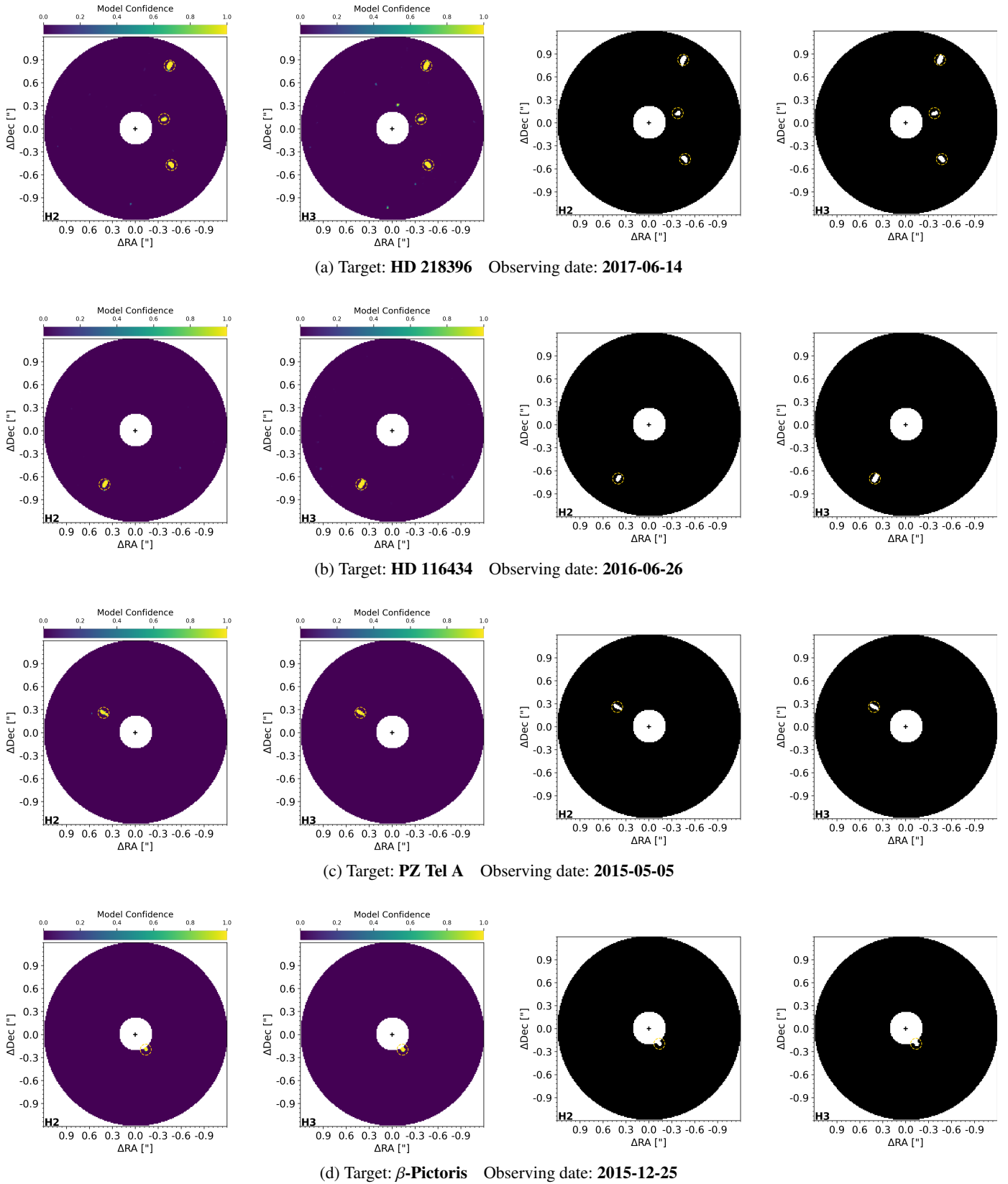


Fig. B.1: Detection maps for a selection of F150 targets where NA-SODINN identifies confirmed substellar companions. Each horizontal panel corresponds to a different target, as indicated below the panel, and includes four sub-maps: the two on the left show NA-SODINN confidence maps for the H2 and H3 filters, while the two on the right display the corresponding F_1 (binary) maps, generated by applying the computed threshold mask to the confidence maps (see Section 3.4.2). In each sub-map, the companion is indicated with a small dashed circle in yellow, the filter used is indicated in the bottom-left corner, and the central masked region corresponds to the inner working angle. The field orientation is standard: north is up and east is to the left.

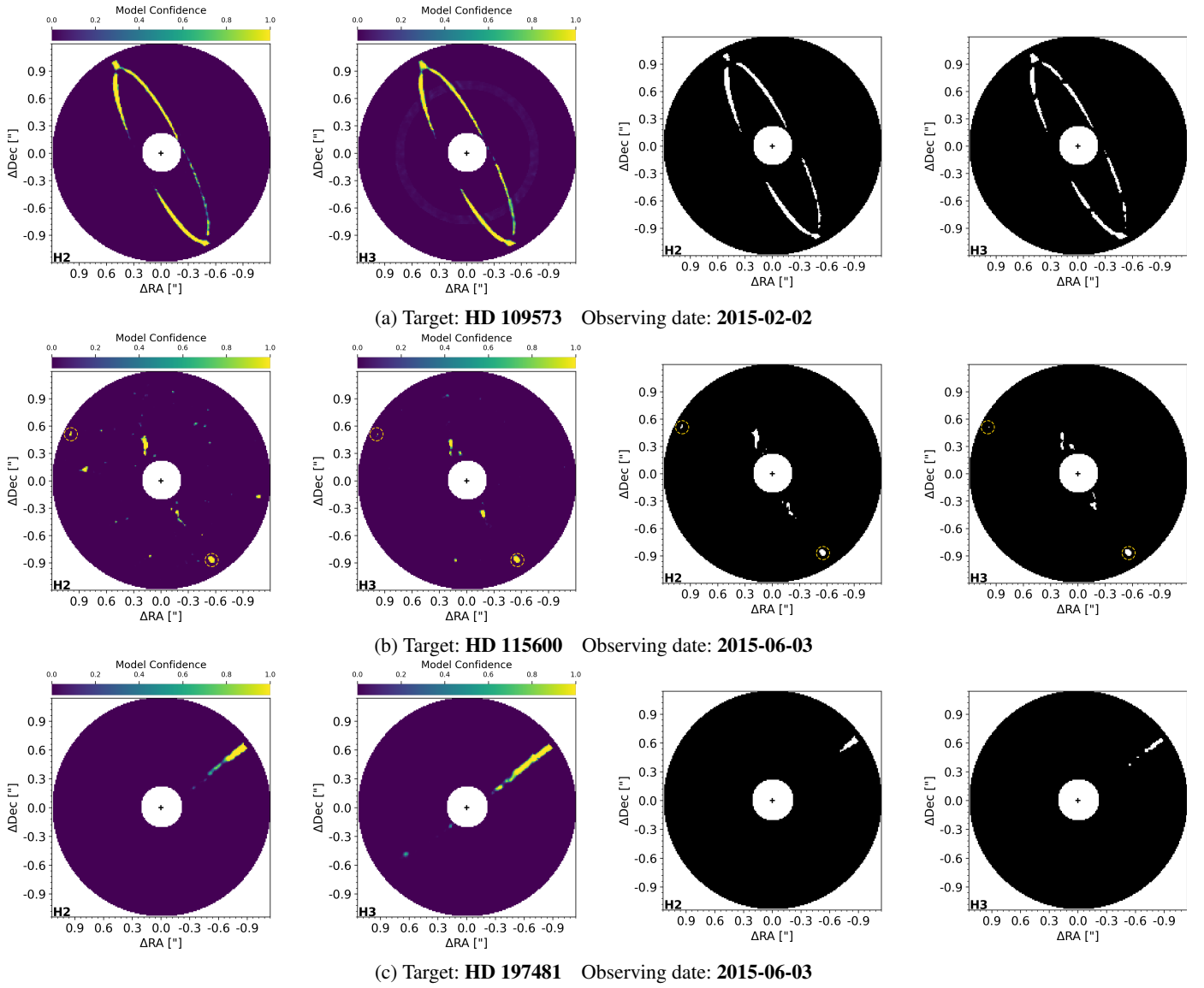


Fig. B.2: Detection maps for the F150 sample targets in which NA-SODINN recovers known protoplanetary disks. For HD 115600 (middle panel), the two sources at large angular separations (highlighted with yellow circles), located outside the inner disk, were previously classified as background contaminants (Langlois et al. 2021; Chomez, A. et al. 2025). The structure and interpretation of this figure follow the same format as in Fig. B.1.

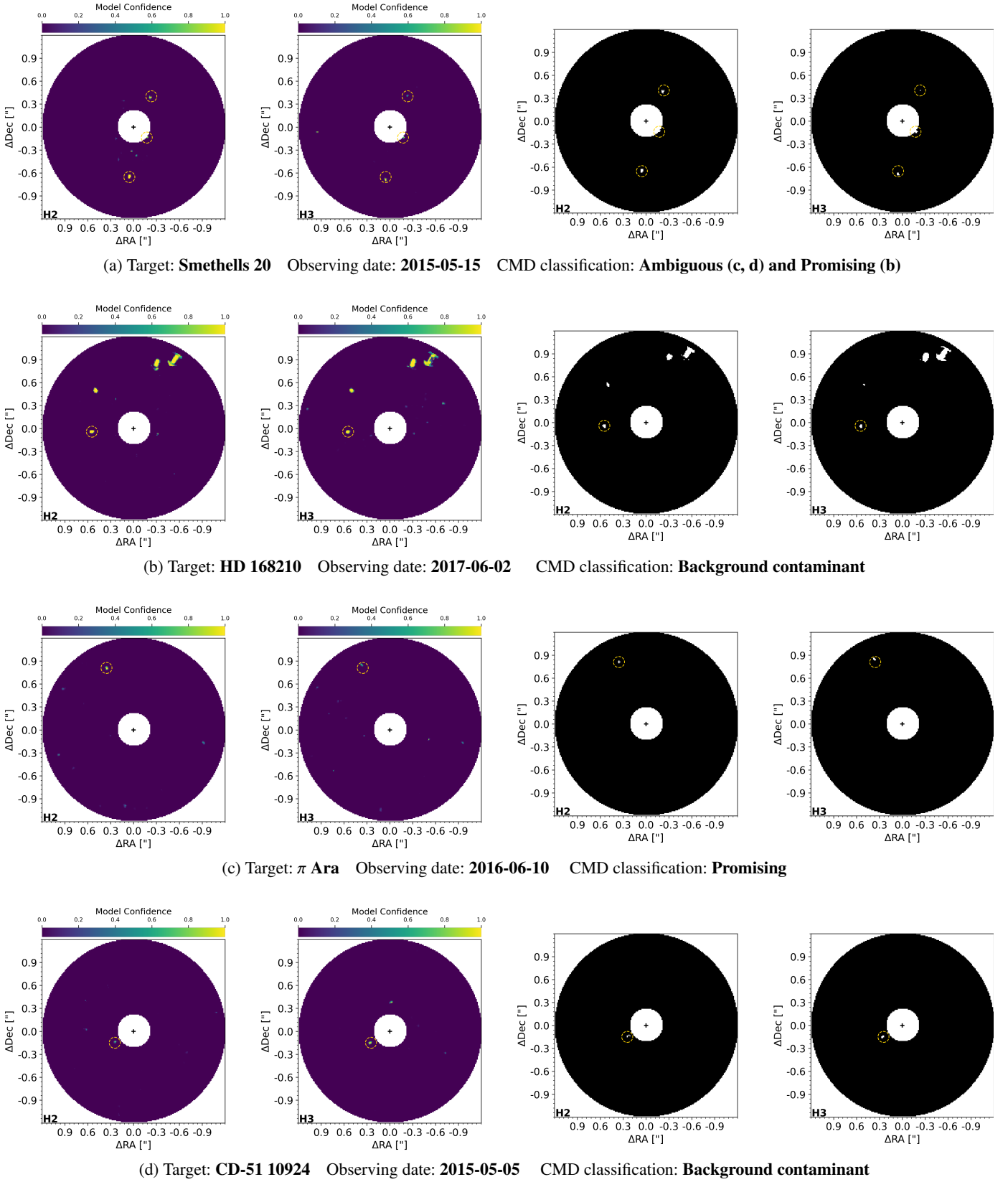
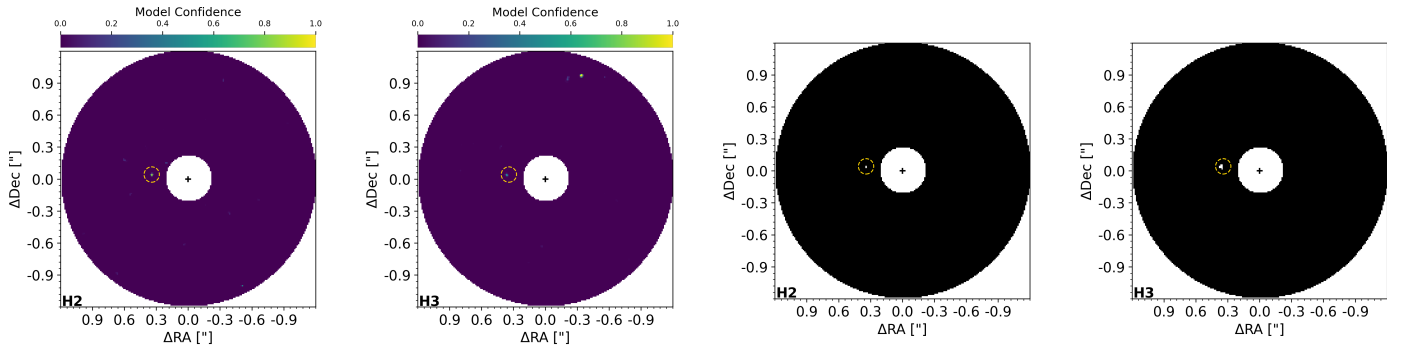
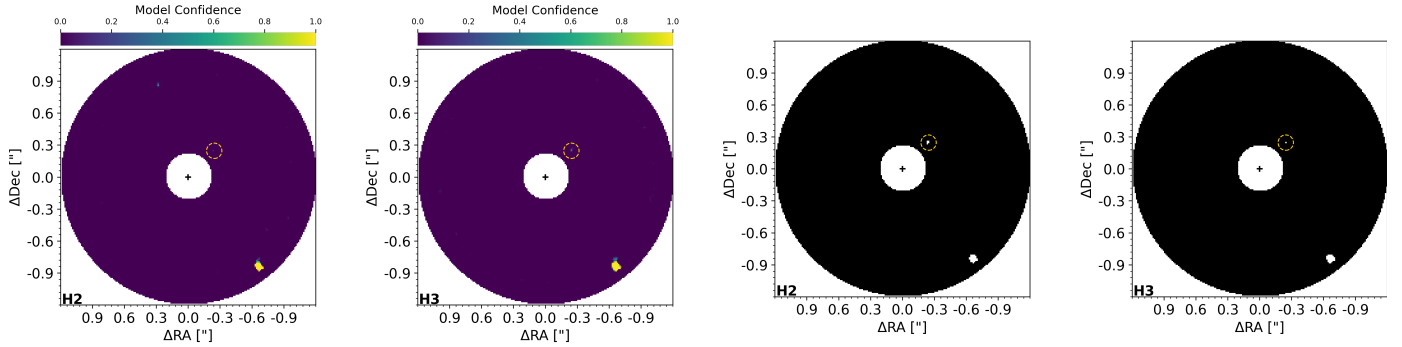


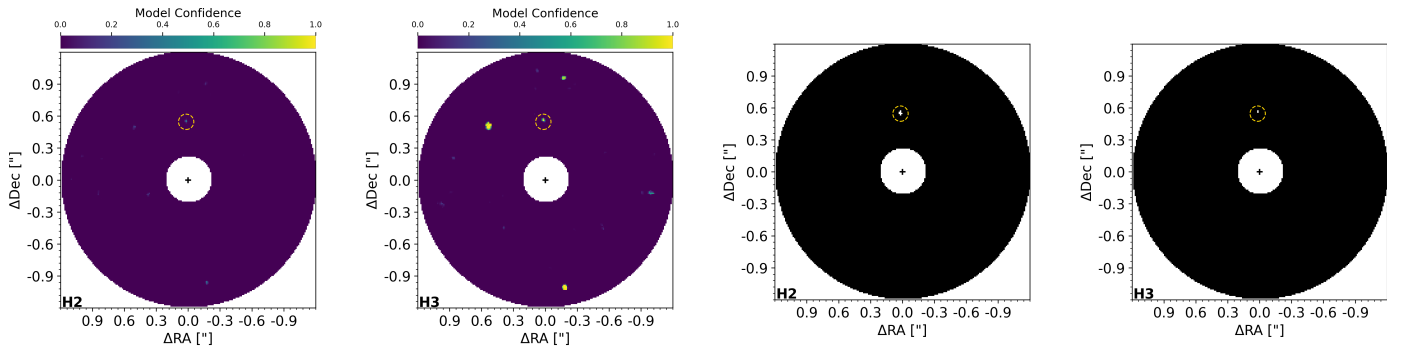
Fig. B.3: Detection maps for F150 sample targets where NA-SODINN identifies new candidates, yet unreported, detected in both the H2 and H3 pass-band filters. For HD 168210 (second panel), the three additional detections at large separations (without circle) were also classified as ambiguous cases (Langlois et al. 2021; Chomez, A. et al. 2025). Both the reference labels and the characterization of these detections can be found in Table C.2. The structure and interpretation of this figure follow the same format as in Fig. B.1.



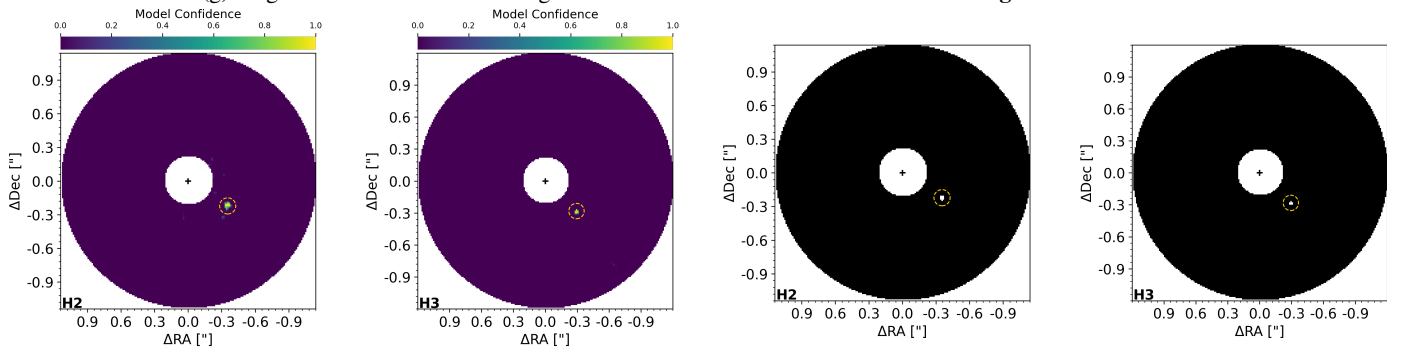
(e) Target: β Leo Observing date: 2015-05-30 CMD classification: **Background contaminant**



(f) Target: HD 164249 Observing date: 2018-04-10 CMD classification: **Promising**



(g) Target: CD-57 1054 Observing date: 2016-01-02 CMD classification: **Background contaminant**



(h) Target: CE Ant Observing date: 2017-02-06 CMD classification: **Background contaminant**

Fig. B.3: Continuation. For HD 164249 (second panel), the candidate at large separation (without circle) was also classified as background contaminant (Langlois et al. 2021; Chomez, A. et al. 2025).

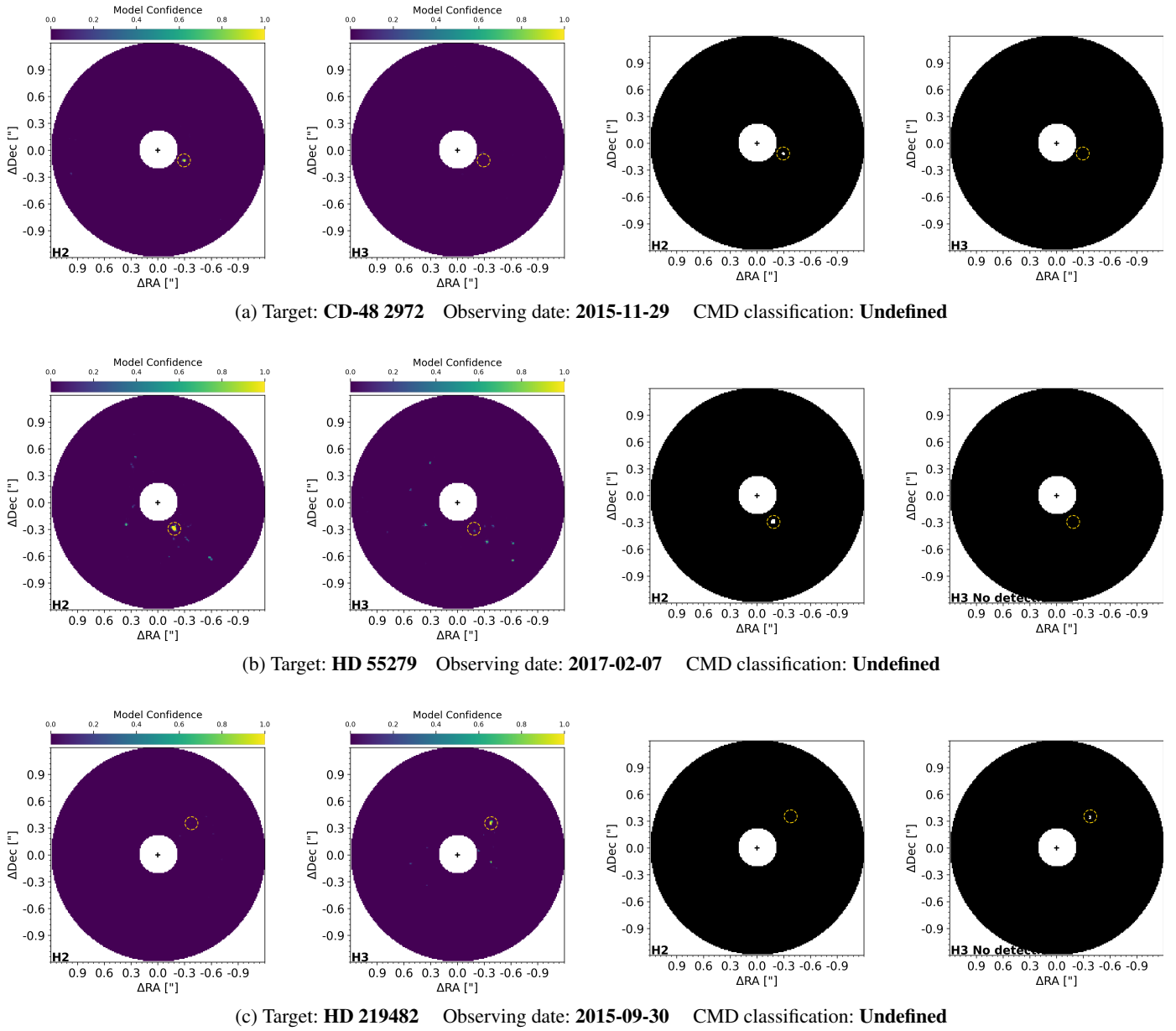


Fig. B.4: Detection maps for F150 sample targets where NA-SODINN identifies new companion candidates, detected in only one of the two passband filters (H2 or H3). The characterization of these detections can be found in Table C.2. The structure and interpretation of this figure follow the same format as in Fig. B.3.

Table C.1: Properties of the 11 targets around which NA-SODINN identified new companion candidates. The top panel shows targets with candidates detected in both the H2 and H3 filters, while the bottom panel shows targets with candidates detected in only one of the two filters. The two panels are ordered by decreasing right ascension (RA).

Main Name	Other-ID	Gaia-ID	RA	DEC	H mag	Sp. type	Age [Myr]	Distance [pc]
CD-57 1054	HIP 23309	4764027962957023104	05:00:47	-57:15:25	6.42	M0V	$24 \pm 5^{(1)}$	26.86
CE Ant	TWA 7	5444751795151480320	10:42:30	-33:40:17	7.12	M2V	$10 \pm 3^{(1)}$	34.10
β -Leo	HIP 57632	-	11:49:03	+14:34:19	1.92	A3V	$50 \pm 10^{(1)}$	11.00
CD-51 10924	HIP 85647	5925209583053212800	17:30:11	-51:38:13	6.08	M0V	15.3	15.98
π -Ara	HIP 86305	5921246427739258112	17:38:05	-54:30:01	4.86	A7V	$570 \pm 210^{(2)}$	41.01
HD 164249	HIP 88399	6702775135228913280	18:03:03	-51:38:56	6.02	F6V	15.3	49.30
HD 168210	HIP 89829	4051081838710783232	18:19:52	-29:16:33	7.19	G5V	$24 \pm 5^{(1)}$	80.46
Smethells 20	TYC 9073-762-1	6631685008336771072	18:46:52	-62:10:36	8.04	M1V	$24 \pm 5^{(1)}$	50.69
HD 55279	HIP 33737	5208216951043609216	07:00:30	-79:41:45	7.83	K2V	$45 \pm 10^{(1)}$	63.45
CD-48 2972	TYC 8128-1946-1	5506101790904438656	07:28:22	-49:08:37	8.13	G8V	$50 \pm 10^{(1)}$	87.21
HD 219482	HIP 114948	6489909443564308224	23:16:57	-62:00:04	4.60	F6V	$300 \pm 150^{(2)}$	20.44

References. Ages are adopted from different sources: (1) based on membership in moving groups, associations, or clusters; (2) from [Desidera et al. \(2021\)](#). Distances are derived from *Gaia* parallaxes.

Table C.2: Characterization of the newly identified candidates detected by NA-SODINN, as shown in Figs. B.3 and B.4. The table is divided into eleven sections, each corresponding to a target listed in Table C.1, around which one or more companions are identified. The column CMD reports the candidate classification based on the analysis in Section 4.2.

Candidate ID	Band	Separation [mas]	Position angle [°]	Contrast	Δ mag	CMD
Smethells 20						
b	H2	218.94 ± 30.02	323.35 ± 7.31	$1.04 \pm 0.55 \times 10^{-4}$	9.95 ± 0.65	Promising
	H3	227.59 ± 29.21	322.37 ± 7.09	$7.65 \pm 3.87 \times 10^{-5}$	10.29 ± 0.69	
c	H2	448.36 ± 30.64	60.65 ± 3.51	$2.68 \pm 1.43 \times 10^{-5}$	11.33 ± 0.79	Ambiguous
	H3	462.80 ± 30.05	60.46 ± 3.27	$2.39 \pm 1.53 \times 10^{-5}$	11.42 ± 0.74	
d	H2	664.86 ± 28.94	264.69 ± 2.35	$2.55 \pm 1.59 \times 10^{-5}$	11.34 ± 0.72	Ambiguous
	H3	700.81 ± 29.74	264.32 ± 2.29	$1.83 \pm 1.03 \times 10^{-5}$	11.91 ± 0.83	
HD 168210						
b	H2	569.35 ± 21.03	185.00 ± 1.10	$3.82 \pm 2.17 \times 10^{-6}$	13.55 ± 0.61	Background
	H3	568.91 ± 26.80	185.15 ± 2.55	$5.33 \pm 2.42 \times 10^{-6}$	13.19 ± 0.50	
π Ara						
b	H2	888.45 ± 21.75	114.26 ± 1.16	$6.31 \pm 2.85 \times 10^{-6}$	13.00 ± 0.51	Promising
	H3	920.71 ± 25.46	114.36 ± 1.28	$4.67 \pm 3.24 \times 10^{-6}$	13.33 ± 0.79	
CD-51 10924						
b	H2	280.09 ± 27.01	210.62 ± 5.14	$2.22 \pm 1.43 \times 10^{-5}$	11.63 ± 0.74	Background
	H3	294.78 ± 26.33	210.21 ± 4.27	$1.46 \pm 0.91 \times 10^{-5}$	12.08 ± 0.76	
β Leo						
b	H2	370.09 ± 23.98	175.30 ± 2.87	$1.48 \pm 0.62 \times 10^{-5}$	12.07 ± 0.50	Background
	H3	377.84 ± 24.67	178.50 ± 4.15	$2.68 \pm 1.15 \times 10^{-5}$	11.43 ± 0.47	
HD 164249						
b	H2	330.35 ± 30.77	47.21 ± 5.09	$2.66 \pm 1.13 \times 10^{-5}$	11.43 ± 0.74	Promising
	H3	341.74 ± 31.05	46.26 ± 4.58	$1.97 \pm 0.87 \times 10^{-5}$	11.34 ± 0.79	
CD-57 1054						
b	H2	552.91 ± 30.26	92.61 ± 2.74	$7.60 \pm 3.78 \times 10^{-6}$	12.80 ± 0.52	Background
	H3	560.06 ± 29.50	92.32 ± 2.51	$6.95 \pm 4.12 \times 10^{-6}$	12.90 ± 0.68	
CE Ant						
b	H2	413.34 ± 28.64	328.7 ± 3.79	$4.20 \pm 1.97 \times 10^{-6}$	13.43 ± 0.62	Background
	H3	423.69 ± 28.97	328.36 ± 3.68	$3.90 \pm 1.80 \times 10^{-6}$	13.53 ± 0.51	
CD-48 2972						
b	H2	305.32 ± 31.39	337.29 ± 5.55	$1.73 \pm 1.01 \times 10^{-5}$	11.90 ± 0.63	Undefined
HD 55279						
b	H2	318.60 ± 27.84	302.87 ± 4.23	$2.91 \pm 1.57 \times 10^{-5}$	11.34 ± 0.62	Undefined
HD 219482						
b	H3	399.89 ± 24.64	47.17 ± 3.22	$2.00 \pm 1.23 \times 10^{-6}$	14.23 ± 0.75	Undefined